Systematic analysis of *C. elegans* embryo behavior reveals a stereotyped developmental progression and a rhythmic pattern of behavioral quiescence

Evan L. Ardiel[1,2,7], Andrew Lauziere[3,4,7], Stephen Xu[3], Brandon J. Harvey[3,5], Ryan Christensen[3], Stephen Nurrish[1,2], Joshua M. Kaplan[1,2,8,*], Hari Shroff[3,6,8]

[1]Department of Molecular Biology, Massachusetts General Hospital, Boston, MA, 02114, USA

[2]Department of Neurobiology, Harvard Medical School, Boston, MA, 02115, USA

[3]National Institute of Biomedical Imaging and Bioengineering, National Institutes of Health, Bethesda, MD, 20814, USA

[4]Department of Mathematics, University of Maryland, College Park, MD, 20742, USA

[5]Current address: Department of Neurology, Emory University, Atlanta, GA, 30322, USA

[6]Fellows Program, Marine Biological Laboratory, Woods Hole, MA, 02543, USA

[7]These authors contributed equally

[8]Senior author

[*]Correspondence: kaplan@molbio.mgh.harvard.edu

Abstract

Systematic analysis of rich behavioral recordings is being used to uncover how circuits encode complex behaviors. Here we apply the approach to embryos. What are the first embryonic behaviors and how do they evolve as early neurodevelopment ensues? To address these questions, we present a systematic description of behavioral maturation for *Caenorhabditis elegans* embryos. Posture libraries were derived from a genetically encoded motion capture suit imaged with light-sheet microscopy and annotated using custom semi-automated tracking software (Multiple Hypothesis Hypergraph Tracking; MHHT). Analysis of cell trajectories, postures, and behavioral motifs revealed a stereotyped developmental progression. Early movement is dominated by flipping between dorsal and ventral coiling, which gradually slows into a period of reduced motility. Late-stage embryos exhibit sinusoidal waves of dorsoventral bends, prolonged bouts of directed motion, and a rhythmic pattern of pausing, which we designate slow wave twitch (SWT). Synaptic transmission is required for late-stage motion but not for early flipping or the intervening inactive phase. A high-throughput behavioral assay and calcium imaging revealed that SWT is elicited by the rhythmic activity of a quiescence-promoting neuron (RIS). Similar periodic quiescent states are seen prenatally in divergent animals and may play an important role in promoting normal developmental outcomes.

Introduction

The set of synaptic connections assembled during development form a physical substrate for brain activity, behavior, and cognition. Diverse model systems have been deployed to identify the molecular components essential for initiating this process, from neuronal differentiation to synaptogenesis. In parallel, postnatal behaviors have been studied from genes to cells to circuits. By comparison, few datasets bridge these lines of inquiry, i.e., probe the emergence of functional neural circuitry. New principles are likely to be discovered through focused analysis of nascent neuronal circuits and the behaviors they elicit. Indeed, the structural remodeling of synapses peaks early and becomes less dynamic with age and the maturation of some circuitry is restricted to specific stages (critical periods) early in development (Hensch, 2004).

In 1695, Antonie van Leeuwenhoek expressed his amazement at first seeing motility in unborn mussels, writing that the graceful rotations were beyond comprehension. Careful observation has since uncovered details of embryonic behavior across phylogeny (Preyer, 1885). Studies of the chick embryo were particularly influential, where it was established that rhythmic muscle contractions were mediated by stereotyped spontaneous activity in neuromuscular circuitry (Hamburger, 1963). Behavioral classification has traditionally relied on expert observers; however, new tools for data-driven analysis of rich behavioral recordings are accelerating progress in ethology and systems neuroscience (Berman, 2018; Brown & de Bivort, 2018; Datta et al., 2019; Pereira et al., 2020). Applying this approach to embryos has the potential to answer several questions about early brain development. What are the first behaviors embryos exhibit? Is there a stereotyped developmental progression for these

behaviors? Is this progression dictated by the timing of ongoing neurodevelopment (i.e. circuit wiring)? Do embryonic circuits encode behaviors by mechanisms distinct from those found in mature, post-natal circuits?

To address these questions, here we build a comprehensive picture of embryonic behavior in the microscopic roundworm *Caenorhabditis elegans. C. elegans* offers several advantages for investigating the emergence of functional neuronal circuitry and behavior. Embryos are small (~50x30x30 μm^3) and transparent, enabling in vivo imaging of cell migration, neurite growth, synaptogenesis, neuronal activity, and behavior during the mere ~14 hours from fertilization to hatching (Shah et al., 2017; Barnes et al., 2020; Heiman & Shaham, 2009; Fan et al., 2019; Christensen et al., 2015; Moyle et al., 2020; McDonald et al., 2020; Sengupta et al., 2020; Ardiel et al., 2017; Hall & Hedgecock, 1991; Atakan et al., 2020; Bayer et al., 2021). *C. elegans* boasts a sophisticated molecular genetic toolkit, a complete neuronal wiring diagram, and a comprehensive atlas of single cell gene expression across embryogenesis (White et al., 1986; Cook et al., 2019; Witvliet et al., 2021; Packer et al., 2019). *C. elegans* has been a powerful system for analyzing circuits and behavior; however, virtually all such studies have focussed on post-embryonic stages, including “cradle to grave” behavioral recordings (Stern et al., 2017; Churgin et al., 2017). In embryos, cell movement has been fully tracked from the first cell division up to the first muscle contraction, which occurs at about 430 minutes post-fertilization (mpf; Bao et al., 2006; Giurumescu et al., 2012; Kumar et al., 2016). Tracking movement beyond this point is complicated by the embryo’s rapid transitions between entangled body postures. At hatching, the 222-cell larval nervous system already supports directed locomotion and even learning and memory (Hong et al., 2017). Thus, a functional

89 motor program emerges over what is arguably the least documented 6 hours of the worm's life
90 (430-800 mpf).

91 It is currently not known when the nervous system begins generating behavior. Pre-
92 synaptic proteins are first localized in the worm's "brain", a large circumferential bundle of
93 axons called the nerve ring, less than an hour before the first muscle contraction (McDonald et
94 al. 2020). However, these pre-synaptic proteins exhibit high diffusional mobility at this stage
95 (McDonald et al. 2020) and it is unclear when nerve ring synapses become functional. Mutants
96 lacking essential muscle genes arrest as two-fold embryos, indicating that muscle contractions
97 are required for elongation of the embryo's body (Williams & Waterston, 1994). Elongation is
98 unaffected in mutants deficient for neuronal function, implying that initial muscle contractions
99 do not require neuronal input. In a developmental series of electron micrographs, pre-synaptic
100 vesicle clusters at body wall neuromuscular junctions are first observed at ~550 mpf (Durbin,
101 1987). In late-stage embryos, backward locomotion correlates with activity of backward
102 command interneurons (Ardiel et al., 2017), suggesting the existence of a functional motor
103 program prior to hatching. Here we documented all postural transitions for the final 4.5+ hours
104 of embryogenesis (530 mpf to hatching). We find that embryos exhibit a stereotyped pattern of
105 behavioral maturation, including a period of rhythmic quiescence. This rhythmic quiescence is
106 elicited by the RIS neuron, which promotes sleep-like behaviors in larvae and adults (Turek et
107 al., 2013; Wu et al., 2018). Rhythmic sleep-like states are a highly conserved feature of prenatal
108 behavior (Balaban et al., 2012; Pereanu et al., 2007; Okai et al., 1992; Szeto & Hinman, 1985;
109 Corner, 1977). *C. elegans* offers a powerful system for investigating this phenomenon from
110 genes to cells to circuits.

Results

Building embryo posture libraries

To model posture, we tracked the location of the paired skin cells that run along the left and right sides of the *C. elegans* embryo, hereafter designated seam cells. GFP-expressing seam cell nuclei were imaged by light-sheet fluorescence microscopy, which allows rapid optical sectioning with minimal photodamage. With single view imaging (iSPIM; Wu et al., 2011; Kumar et al., 2015), we recorded volumes at 3 Hz for more than 4.5 hours without delaying the timing of the Q/V5 cell division (~695-725 mpf) or hatching (<820 mpf; Fig. 1a). Following image acquisition, all seam cell nuclei were tracked across more than 50,000 image volumes (>1 million links per embryo; Fig. 1b, Movie 1). To optimize nucleus detection, we compared several segmentation methods in manually annotated image volumes. The best performance was obtained using a 3D convolutional neural network (Supplementary Note).

We developed Multiple Hypothesis Hypergraph Tracking (MHHT) to link seam cells across image volumes. Due to the embryo's anatomy, seam cell movements are correlated and distances between neighboring cells are constrained (Fig. 1c, Supp. Fig. S1). MHHT leverages these interdependencies to facilitate semi-automated tracking that is robust to imperfect detections. In Multiple Hypothesis Tracking (MHT), the top *K* assignments for minimizing frame-to-frame movement are evaluated over *N* frames (Reid, 1979; Cox & Hingorani, 1996). MHHT extends MHT by using empirically derived covariances to assign costs to competing cell assignment hypotheses based on their deviation from expected motion patterns. Using a depth-first search, MHHT identifies the cell assignment hypothesis that has the lowest cost accrued over *N* frames, disregarding branches that generate physically impossible body

133 contortions (i.e., body segments passing through one another; Fig. 1d). For a ground truth
134 dataset in which all seam cell detections were confirmed by expert observers, MHHT failed to
135 correctly assign at least one seam cell in only 1.46% of 51,553 image volumes (for *K*=5, *N*=3), a
136 27.2% reduction in error rate compared to using global nearest neighbor tracking (GNN, i.e.,
137 *K*=1, *N*=1). Error rates increase considerably for non-curated datasets with missing or false cell
138 detections. Using our best detection method (3D U-Net; Cicek et al., 2016), MHHT failed to
139 correctly assign at least one seam cell in 6.52% of 51,553 image volumes (for *K*=25, *N*=2), a
140 14.2% reduction in error rate compared to GNN. MHHT notifies users when a cost threshold is
141 crossed, allowing for manual editing of cell assignments before resuming automated tracking. A
142 detailed description of MHHT is provided in Supplementary Note and the code is freely
143 available at https://github.com/lauziere/MHHT. Collectively, these methods (iSPIM, 3D U-Net
144 segmentation, and MHHT) comprise a semi-automated pipeline for documenting embryonic
145 posture. We generated a comprehensive catalogue of postural transitions for three control
146 embryos, recording the position of all seam cells three times per second from 530 mpf to hatch
147 (>4.5 hours). These 150,000+ annotated image volumes (available on FigShare,
148 https://figshare.com/s/6d498d74f98cca447d41) create a new resource for the systematic
149 analysis of embryo behavior.
150

151 **Eigen-embryos compactly describe posture and behavioural motifs**

152 Adult worms crawling on a 2D agar surface explore a low dimensional postural space.
153 Stephens et al. (2008) found that over 90% of variance in dorsoventral bending along the
154 midline could be accounted for with just 4 principal components (PCs), which they termed

155 “eigenworms”. To determine if embryo postures could be similarly described, we used seam
156 cell positions to fit each side of the body with a natural cubic spline and then computed
157 dorsoventral bending angles between adjacent seam cells (totalling 18 bends in each volume;
158 Fig. 2a, b). Four PCs captured over 88% of the variance in this metric (Fig. 2c, d). The
159 eigenvectors of these four components (termed eigen-embryos) were stereotyped between
160 animals, with PC1 for example capturing ventral or dorsal coiling and PC2 describing postures
161 with opposing anterior and posterior bends (Fig. 2e). In this framework, any embryonic posture
162 can be described by a linear combination of eigen-embryos. PC2 and PC3 approximate sinusoids
163 with a phase difference of 90° (a quadrature pair), which can be combined to generate
164 travelling waves. The contribution of eigen-embryos shifted consistently across development,
165 with less variance accounted for by PC1, as PC2 and PC3 gained prominence (Fig. 2d).
166 Consistent with behavioral maturation, the developmental shift towards PC2 and PC3 better
167 aligns eigen-embryos with eigenworms, for which the top two PCs jointly approximate a
168 quadrature pair (Stephens et al., 2008). The relatively limited dimensionality of dorsoventral
169 bending observed in both adults and embryos is likely a consequence of muscle anatomy, with
170 electrically coupled muscle bundles running ventrally and dorsally along the body (White et al.,
171 1986).
172 Owing to the bilateral symmetry of seam cells, we could not assign left versus right
173 identity and consequently could not distinguish dorsal from ventral bending. Given the
174 differential neuronal input to dorsal and ventral muscles (White et al., 1978; Hallam & Jin,
175 1998), we wondered whether embryos developed a systematic asymmetry in postures. Indeed,
176 a coiling bias was apparent early versus late in all three embryos, as indicated by the tails of the

177 PC1 amplitude distribution (Supp. Fig. S2a). To determine whether this bias was consistently
178 dorsal or ventral, we acquired a supplemental dataset of 16 embryos in which additional
179 fluorescent markers were imaged at higher spatial resolution. In these image volumes, left and
180 right seam cell nuclei could be unambiguously distinguished by manual inspection. The low
181 temporal resolution of this supplemental dataset (5 min intervals) precluded behavioural
182 tracking; however, the postures exhibited by these embryos were described by a similar set of
183 eigen-embryos (Supp. Fig. S2c) and revealed a dorsal coil bias in the final hours of
184 embryogenesis (Supp. Fig. S2b). By assuming a late-stage dorsal coil bias we were able to assign
185 left and right identity to seam cells in the three embryos recorded at 3 Hz.
186 Using differential interference contrast **(**DIC) microscopy and manual visual inspection,
187 Hall & Hedgecock (1991) published one of the few reports on *C. elegans* embryonic behavior.
188 They describe embryo motion as flips about the anteroposterior axis that decline in frequency
189 ahead of the emergence of the "larval locomotor pattern". This developmental progression was
190 readily apparent in posture space. Flips about the anteroposterior axis were seen as oscillating
191 PC1 amplitudes, which signifies alternating dorsal and ventral coiling (Fig. 2f; Supp. Fig. S2d, e).
192 The "larval locomotor pattern" was best captured by PC2 and PC3 amplitudes, for which phase-
193 shifted cycling describes dorsoventral bend propagation along the body axis, reminiscent of
194 sinuous crawling (Fig. 2f; Supp. Fig. S2f). Thus, the posture library captures a developmental
195 progression from immature (dorsoventral flipping) to mature (sinusoidal crawling) embryo
196 behavior.
197
198 **Assessing speed, direction of motion, and bout durations**

199 Mean squared displacement (MSD) is commonly used to derive descriptive metrics and
200 categorize motion of particles and cells. Consistent with confinement, MSD of embryonic seam
201 cell nuclei saturated in minutes, with the highest plateaus (corresponding to the anteriormost
202 cells) approximating the square of the mean radius of the egg (Fig. 3a). Thus, the embryo's
203 anterior end explores the full eggshell volume. A "diffusion coefficient" (*D*) was estimated by
204 linear fit over 0 to 10 s time lags (30 frames), revealing greater motility for anterior than
205 posterior seam cells (Fig. 3b). We also observed a consistent developmental shift, with the least
206 motility around 600 mpf (Fig. 3c). Fig. 3d highlights the developmental transitions of an anterior
207 (H1) and posterior (V6) seam cell. As predicted from their MSD (Fig.3a), H1 visits the full extent
208 of the eggshell, while V6 is more confined. Note that while the "diffusion coefficients" for the
209 H1 nucleus are virtually identical at 530 and 750 mpf, the trajectories reveal distinct modes of
210 motion, consistent with the different postures found at these time points (Fig. 2d).
211 To further characterize embryo movement, we considered speed and directional
212 persistence. For embryo speed, we measured displacement of left-right seam cell pair
213 midpoints (H1 to V5) over 1 s (3 frames), and then calculated a weighted average based on the
214 straight-line length of the body at that segment and volume (Fig. 3e). Embryo speed varied with
215 age, mirroring the developmental shift in seam cell diffusion coefficients described above (Fig.
216 3c, e). The coefficient of variation in embryo speed highlights the extent to which movement
217 becomes increasingly punctuated in the final hours of embryogenesis (Fig. 3f), with both big
218 displacements and periods of relative inactivity (Fig. 3e). To estimate directional persistence,
219 we scored and timed movements along the anteroposterior axis (see θ in Fig. 3d). Forward and
220 backward movement were defined as $\overline{\theta}$ less than 45 ^{o} or greater than 135°, respectively (Fig.

221 3e). Persistence in both directions increased over the final two hours of embryogenesis (Fig.
222 3g). In summary, our analysis reveals a consistent developmental progression in embryo
223 behavior. Immature embryos flip between dorsal and ventral coiling with near continual
224 motion, while mature embryos show increased directional persistence and pausing, with the
225 transition from immature to mature marked by a period of relative inactivity.
226
227 **Synaptic signalling is required for mature motion, but not dorsoventral flipping**
228 With a bias for dorsal coiling, sinuous crawling, and increasingly directed movement,
229 late-stage embryos exhibit several potential signatures of neuronal influence. To establish a
230 role for synaptic signalling, we analyzed *unc-13*(*s69*) mutants, which have a nearly complete
231 block in synaptic vesicle fusion (Richmond et al., 1999). These mutants are essentially paralyzed
232 after hatching. In late-stage embryos (750 mpf), *unc-13* mutant movement was also strongly
233 impaired, as seen in shorter cell trajectories and smaller diffusion coefficients (Fig. 4a). By
234 contrast, at 530 mpf, seam cell diffusion coefficients for *unc-13* mutants were indistinguishable
235 from controls (Fig. 4b). To search for more subtle defects, we considered the most salient
236 behavior at this stage, i.e., flips about the anteroposterior axis. At 530 mpf, control and *unc-13*
237 mutants were flipping between fully dorsally and fully ventrally coiled postures 3 to 4 times per
238 minute, with 75% of the transitions executed in under 10s (Fig. 4c). Flips can be considered
239 translations along the PC1 axis (Fig. 2f, Supp. Fig. S2d, e) and sub-categorized based on PC2 and
240 PC3 amplitudes during the transition, in this case by the larger absolute mean (PC2 or PC3) and
241 the sign of that mean (- or +). Considering 4 motifs (PC2-, PC2+, PC3-, and PC3+), we found that
242 trajectories through posture space were similarly distributed in control and *unc-13* mutants. For

243 example, ventral to dorsal flips most often initiated in the tail, with intermediate postures
244 having posterior dorsal bending (i.e., the PC2- motif; Fig. 4d). Fig. 4e summarizes the prevalence
245 of each flip motif. Note that dorsal to ventral flips were also more likely to initiate in the tail
246 (i.e., the PC2+ motif; Fig. 4e). This was unexpected, as locomotion after hatching (and in older
247 embryos; Supp. Fig. S2f) is dominated by bends propagating from head to tail, likely requiring
248 neuronal coordination. These results suggest that motion in immature embryos is largely
249 independent of UNC-13-mediated synaptic transmission, although an immature form of
250 synaptic transmission (not requiring UNC-13) cannot be ruled out.
251
252 **A high-throughput brightfield assay for embryonic twitching**
253 To accelerate mutant analysis, we devised a high throughput assay to quantify the
254 twitching structure of late-stage embryogenesis. Brightfield images of up to 60 embryos were
255 acquired at 1 Hz, with frame-to-frame changes in pixel intensity used as a proxy for movement
256 (Fig. 5a, Movie 2). The resulting twitch profiles were highly stereotyped, exhibiting three salient
257 phases: an immature active phase, followed by a period of relative inactivity, followed by an
258 active phase characterized by a broadened distribution of movement magnitudes (Fig 5b, Supp.
259 Fig. S3a). Thus, the motion profile observed in the brightfield assay resembles that derived from
260 seam cell tracking. The similarity in the developmental progression of behavior obtained by
261 these disparate methods confirms that the iSPIM imaging regime was non-invasive and
262 validates the use of the high-throughput brightfield assay to screen for mutants altering
263 embryo behavior.

264 In the frequency domain, we detected an *unc-13* dependent signal in the wild-type
265 scalogram: a 20-40 mHz feature in the final 1-2 hours ahead of hatching (Fig. 5c, d, Supp. Fig.
266 S3b). We call this feature "slow wave twitch" or SWT. In *unc-13* mutants, peak SWT power
267 ratios were markedly diminished compared to wild-type (Fig. 5e) and failed to localize to a
268 specific developmental stage (Fig. 5d). Thus, SWT represents a rhythmic embryonic behavior
269 with a period of 25-50 seconds that depends on synaptic transmission.
270 To probe the neuronal underpinnings of SWT, we evaluated mutants perturbing specific
271 neurotransmitters. Peak SWT power ratios were unaffected by loss of the vesicular transporters
272 for biogenic amines (CAT-1/VMAT), glutamate (EAT-4/VGLUT), or GABA (UNC-47/VGAT). By
273 contrast, peak SWT power ratios but were strongly diminished in mutants lacking the vesicular
274 transporter for acetylcholine (UNC-17/VAChT; Fig. 5e), indicating that cholinergic transmission
275 plays a prominent role in generating SWT. Body wall muscles express two classes of nicotinic
276 acetylcholine receptors: homopentameric ACR-16 receptors and heteropentameric levamisole
277 receptors containing UNC-29 subunits (Richmond & Jorgensen, 1999; Touroutine et al., 2005).
278 Mutants lacking UNC-29 had significantly reduced peak power ratios in the SWT frequency
279 band, a defect that was rescued by a transgene expressing UNC-29 in muscle (Fig. 5e). By
280 contrast, peak SWT power ratios were unaffected in *acr-16* mutants (Fig. 5e). Thus, SWT
281 requires cholinergic signalling through UNC-29-containing receptors in muscle. Peak SWT power
282 ratios were also strongly diminished in mutants lacking neuropeptide processing enzymes (EGL-
283 3/PC2 and EGL-21/CPE; Fig. 5e), implicating neuropeptide signalling in SWT.
284
285 **SWT is mediated by FLP-11 release from RIS**

286 The timing of SWT coincides with an increased propensity for pausing (Fig 3e);
287 consequently, we hypothesized that periodic quiescent bouts were generating signal in the 20-
288 40 mHz frequency band. Neuropeptides released from RIS and/or ALA are known to elicit
289 behavioural quiescence in larvae and adults (Turek et al., 2013; Turek et al., 2016; Van Buskirk
290 et al. 2007; Nath et al., 2016). We investigated whether either of these neurons is required for
291 SWT by analyzing mutants lacking RIS (*aptf-1*/AP-2) or ALA (*ceh-17*/PHOX2A) function (Turek et
292 al. 2013; Pujol et al., 2000; Van Buskirk et al. 2007). Consistent with a role for RIS, we found that
293 peak SWT power ratios were markedly reduced in *aptf-1* mutants but were unaffected in *ceh-*
294 *17* mutants (Fig. 6a). The somnogenic neuropeptides released from RIS are encoded by the *flp-*
295 *11* gene (Turek et al., 2016). While their developmental progression was superficially normal in
296 terms of gross movement magnitude, the *flp-11* mutant scalogram lacked an SWT signature
297 (Fig. 6b). Indeed, peak SWT power ratios in *flp-11* mutants were severely diminished compared
298 to wild-type (Fig. 6a). These data suggest that late-stage movement is structured by periodic
299 release of FLP-11 from RIS, specifically increasing power in the 20-40 mHz frequency band.
300 To relate RIS signalling and behavior, we simultaneously monitored RIS motion and
301 activity with a genetically encoded calcium sensor, GCaMP6f (Chen et al., 2013), fused to a
302 calcium insensitive fluorophore, mCherry. Tracking GCaMP/mCherry ratios in the RIS cell body
303 in embryos aged at least 645 mpf (Fig. 6c, d), we observed RIS calcium transients at a rate
304 approximating 20-40 mHz, similar to the SWT frequency band (Fig. 6e). Furthermore, RIS
305 calcium transients correlated with behavioral slowing (Fig. 6g). In mutants lacking FLP-11
306 neuropeptides, RIS activity was unaltered; however, behavioural quiescence was substantially
307 reduced (Fig. 6e,f), as was the negative correlation of RIS calcium transients with motion (Fig.

308 6g). These results suggest that a prominent feature of late-stage embryonic behavior is a
309 rhythmic pattern of quiescence elicited by FLP-11 release from RIS.
310
311 **Discussion**
312 Here we describe a systematic analysis of behavioral maturation in *C. elegans* embryos.
313 Our analysis leads to three principal conclusions. First, embryos follow a stereotyped
314 behavioural trajectory: early flips between dorsal and ventral coiling (most often initiated in the
315 tail) slowing into a period of reduced motility, followed by emergence of mature motion
316 (including sinuous crawling and rhythmic quiescent bouts). Second, synaptic transmission is
317 required for late-stage movement, but not for early dorsoventral flipping or the intervening
318 inactive period. Third, the bouts of behavioral quiescence punctuating late-stage movement are
319 elicited by FLP-11 release from RIS neurons.
320 Flipping between dorsal and ventral coiling dominates early embryo behavior. This
321 behavioral motif is not obviously affected by loss of *unc-13*, implying it does not depend on
322 synaptic transmission. Flipping could be mediated by intrinsic oscillatory activity in muscles or
323 by neuronal signaling that persists in the absence of UNC-13 (e.g. gap junctions or non-
324 conventional synaptic transmitter release). It will be interesting to determine what drives
325 immature flipping and whether this early behavior is required in some way for the subsequent
326 emergence of mature behaviors. Flipping gradually slows into a period of relative inactivity. This
327 slowdown is apparently not neuronally evoked, as it requires neither neuropeptide processing
328 enzymes nor UNC-13. Slowing does coincide with a shift in the forces defining body
329 morphology, from a squeeze generated by contraction of circumferential actin bundles of the

330 epidermal cytoskeleton to containment within a tough, yet flexible extracellular cuticle (Priess
331 & Hirsh, 1986). This structural transition could impact behavior; however, preliminary calcium
332 imaging experiments suggest that at least part of the slowdown can be attributed to reduced
333 muscle activity, rather than simply a structural constraint limiting motion. A shift from
334 cytoskeletal to exoskeletal control of morphology is likely re-iterated at each larval molt and
335 could contribute to molt-associated lethargus quiescence (Raizen et al., 2008). The brightfield
336 motion assay promises to be a useful screening tool to further investigate this phenomenon.
337 We identify SWT as a new form of behavioral quiescence, occurring during
338 embryogenesis. Osmotic stress and reduced insulin signalling cause behavioral quiescence
339 around hatching, which is accompanied by developmental arrest (Bayer et al., 2021). The salt
340 and insulin regulated quiescence and SWT quiescence occur at a similar stage of embryonic
341 development and both require FLP-11, suggesting that these two forms of quiescence are
342 mechanistically related. Other forms of *C. elegans* behavioral quiescence have been described
343 during larval molts (lethargus; Raizen et al., 2008) and in response to nutrient excess (satiety;
344 You et al., 2008), cellular stress (e.g., heat shock; Hill et al., 2014), starvation (Skora et al., 2018;
345 Wu et al., 2018), and physical restraint (Gonzales et al., 2019). Behavioral quiescence has been
346 shown to exhibit sleep-like properties: reversibility, reduced sensitivity to external stimuli,
347 homeostatic regulation, and a stereotyped posture (Raizen et al., 2008; Choi et al., 2013; Iwanir
348 et al., 2013; Cho et al., 2014; Tramm et al., 2014; Nagy et al., 2014; Schwarz & Bringmann,
349 2017). Quiescent states can also share deep molecular conservation with sleep in other
350 systems. For example, regulation by both LIN-42/PERIOD (Konopka & Benzer, 1971; Hardin et
351 al., 1990; Sun et al., 1997; Tei et al., 1997; Monsalve et al., 2011) and AP-2 transcription factors

352 (Mani et al., 2005; Turek et al., 2013; Kucherenko et al., 2016; Hu et al., 2020). Among the
353 different quiescent states, SWT shares several properties with lethargus quiescence. First, both
354 are elicited by RIS release of FLP-11 (Fig 6; Turek et al., 2016). Second, lethargus quiescence
355 coincides with molting (i.e. cuticle replacement), while SWT coincides with the synthesis of the
356 first cuticle. Indeed, the embryonic transcriptional profile from the end of gastrulation to
357 hatching correlates with oscillating gene expression across each larval stage (Meeuse et al.,
358 2020). Together, these similarities suggest that SWT may be akin to the developmentally timed
359 sleep associated with each larval molt.

360 An embryonic quiescent state has several potentially important implications. First, if
361 quiescence is required for normal embryonic development, that could help explain why sleep is
362 ubiquitously conserved. Second, sleep disruption is a common co-morbid symptom in
363 neurodevelopmental disorders, including Autism spectrum disorders (ASD; Wintler et al., 2020).
364 Could disrupted prenatal sleep be a risk factor for ASD? ASD linked genes exhibit peak co-
365 expression in mid-fetal neurons (Parikshak et al., 2013; Willsey et al., 2013; Satterstrom et al.,
366 2020), which has been interpreted to suggest that ASD results from disruption of some aspect
367 of fetal brain development. The precise fetal defects associated with ASD have not been
368 identified, perhaps because the specific circuits exhibiting peak ASD gene co-expression have
369 not been identified. Interestingly, we find that embryonic RIS is among the neurons most
370 enriched for expression of ASD linked gene orthologs (Supp. Fig. S4). Based on these results, we
371 speculate that an important function of ASD linked genes is to promote embryonic sleep
372 behaviors.

How might SWT relate to early brain development? Correlated spontaneous activity is essential for the refinement and maturation of developing neuronal circuitry in a variety of contexts (Kirkby et al., 2013). For example, behavioral maturation of *Drosophila* is dependent on patterned spontaneous neuronal activity in embryos (Crisp et al., 2011; Carreira-Rosario et al., 2021). Could RIS be influencing network connectivity by broadly structuring neuronal activity? Embryonic quiescence may also be a mechanism to preserve energy stores. In this scenario, disrupting sleep could predispose embryos to metabolic stress. Indeed, transcriptional stress responses are associated with sleep disruption in worms, flies, and mice (Sanders et al., 2017; Shaw et al., 2000; Cirelli et al., 2006; Terao et al., 2003; Naidoo et al., 2005). It will be interesting to see whether prenatal metabolic stress alters early brain development.

Despite the presence of many important neurodevelopmental benchmarks, behavior during the final hours of *C. elegans* embryogenesis is largely unexplored. The embryonic posture library described here will provide a resource to test new hypotheses about how (and when) embryonic circuits assemble. Semi-automated tracking with MHHT should accelerate expansion of this resource, with the discovery of new embryonic behaviors providing an entry point to study nascent neuronal circuitry. The potential for recording pan-neuronal activity in unanesthetized embryos executing well-defined behaviors (Ardiel et al., 2017) as a stereotyped connectome emerges (Witvliet et al., 2021), uniquely positions *C. elegans* to investigate fundamental aspects of early brain development.

Methods

Strains and reagents

395 Animals were maintained on nematode growth medium (NGM) seeded with *Escherichia*
396 *coli* (OP50) as described in Brenner (1974). The posture library was built with strain JR667 *unc-*
397 *119*(*e2498*::Tc1); *wIs51*[*SCM*p::GFP + *unc-119*(+)], which expresses GFP in hypodermal seam cell
398 nuclei. For the supplemental postures described in Supp. Fig. S2b, c, *wIs51* was combined with
399 epidermal actin marker, *mcIS50*[*lin-26*p::vab-10(actin-binding domain)::GFP + *myo-2*p::GFP] and
400 one of the following mCherry transgenes: *stIs10131*[*elt-7*p::H1-wCherry *+ unc-119*(+)] (SLS20),
401 *stIs10501*[*ceh-36*p::H1-wCherry::*his-24*p::mCherry *+ unc-119*(+)] (SLS21), *stIs10691*[*ref-1*p::H1-
402 wCherry + unc-119(+)] (SLS22), *nuSi187*[*pat-10*p::NLS-GCaMP::mCherry-NLS] (SLS23), *stIs10138*
403 [*tbx-38*p:: H1-wCherry; *unc-119*(+)] (SLS24), or *stIs10808*[*nob-1*p::H1-wCherry; *unc-119*(+)]
404 (SLS25).
405 The following mutant alleles were used in this study: *unc-13*(*s69*), *unc-47*(*e307*), *unc-*
406 *17*(*e245*), *acr-16*(*ok789*), *unc-29*(*x29*), *glr-1*(*n2461*), *cat-1*(*e1111*), *egl-3*(*n150*), *egl-21*(*n476*),
407 *ceh-17*(*np1*), *aptf-1*(*gk794*), *aptf-1*(*tm3287*), and *flp-11*(*tm2706*).
408 For rescuing *unc-29* expression in muscle, plasmid KP#4524 was generated by inserting
409 the *pat-10* promoter (550 bp), the SV40 nuclear localization sequence, mCherry with introns,
410 the EGL-13 nuclear localization sequence, the *gpd-2* 3' UTR with SL2 acceptor site, *unc-29*
411 cDNA, and the *unc-54* 3' UTR between the SpeI and AgeI sites in pCFJ910.
412 For calcium imaging in RIS, plasmid KP#4525 was generated by inserting the *flp-11*
413 promoter (3159 bp), GCaMP6f with introns, a flexible linker (GSSTSG$(AP)_7$ASEF), mCherry with
414 introns, and the *unc-54* 3' UTR between the SbfI and StuI sites in pCFJ910.

415 The miniMOS method (Frøkjær-Jensen et al., 2014) was used to integrate KP#4524 and
416 KP#4525, generating single copy insertions: *nuTi233*[*pat-10*p::NLS::mCherry::SL2::UNC-29] and
417 *nuTi580*[*flp-11*p::GCaMP6f::mCherry].
418 Embryonic age was determined by measuring the time elapsed since twitch onset
419 (which was defined as 430 mpf).
420
421 **Posture library**
422 Sample preparation: Gravid adults were dissected to release embryos, which were
423 transferred to a patch of poly-L-lysine (1 mg/mL) in a diSPIM imaging chamber filled with M9
424 buffer. Embryo orientation was set to minimize Z-steps, i.e. objective translation along the
425 embryo's minor axis. Prior to fluorescence imaging, brightfield recordings were acquired to
426 stage the embryos.
427 Microscope: On a diSPIM (Kumar et al., 2015), a pair of perpendicular water-dipping,
428 long-working distance objectives (40x, 0.8 NA) were used for brightfield and fluorescence
429 imaging. Acquisition was controlled using Micro-Manager's diSPIM plugin (https://micro-
430 manager.org/). Note that although the diSPIM can collect two orthogonal views, only a single
431 view was used to build posture libraries, i.e. iSPIM mode. Sweeping a 488 nm laser beam
432 (measured <1 µW after the objective), a two-dimensional MEMS mirror in the diSPIM scanhead
433 generated the light-sheet and defined the image volume. To maximize speed, the camera
434 (pco.edge 4.2 or ORCA-Flash 4.0) was oriented such that the chip readout direction was along
435 the embryo's minor axis. The imaging objective was translated in step with the light-sheet,
436 generating 36 planes at a spacing of 1.2 µm. Exposure time per plane was 4 ms and volumes

437 were acquired at 3 Hz. To reduce file size, the camera was set to 4x binning, resulting in 16-bit
438 images with 0.65 μm pixels. See Duncan et al. (2019) for detailed protocols on imaging embryos
439 with the diSPIM.

440 For the supplemental postures described in Supp. Fig. S2b, c, diSPIM acquisition
441 parameters were optimized for spatial resolution rather than speed. Specifically, diSPIM mode
442 was used to acquire image volumes from perpendicular objectives with no pixel binning at the
443 camera. The two orthogonal views were then computationally fused to generate isotopically
444 resolved image volumes (Wu et al., 2013; Guo et al., 2020). Laser power was at least an order of
445 magnitude greater than for the volumes acquired at 3 Hz (i.e., > 30 μW, measured after the
446 objective). The 561 nm laser line was scanned simultaneously, with dual-color image splitters
447 separating detection at the camera (W-VIEW GEMINI, Hamamatsu). Volumes were acquired
448 every 5 minutes from pre-twitching until hatching, with each image volume comprising 50
449 planes at a spacing of 1 μm. Exposure time per plane was 5 ms, with volumes acquired in < 900
450 ms.

451 Analysis:

452 Image volumes were segmented using a large kernel 3D U-Net trained on an average of
453 the Dice coefficient and binary cross-entropy loss functions. See Supplementary Note for
454 additional details on image segmentation. In an early volume with good detections, seam cells
455 were manually positioned along the body axis by observing movement over several frames.
456 From this seed volume, cell position was tracked across time using MHHT. See Supplementary
457 Note and https://github.com/lauziere/MHHT for complete details on MHHT.

458 Left and right seam cells were fit with natural cubic splines using MATLAB's 'cscvn'
459 function. DV bends were then computed from the midpoint (mL/R) along the spline connecting
460 adjacent seam cells and the corresponding midpoint (mR/L) on the opposite side of the body
461 (Fig. 2a). For example, for the DV bend between H0L and H1L:

462 $\vec{v}_1$ connects mL to H0L;

463 $\vec{v}_2$ connects mR to mL;

464 $\vec{v}_3$ connects mL to H1L; and

465 DV bend = arctan2(([$\vec{v}_1$ x $\vec{v}_2$] x [$\vec{v}_2$ x $\vec{v}_3$]) · ($\vec{v}_2$ / |$\vec{v}_2$|), [$\vec{v}_1$ x $\vec{v}_2$] · [$\vec{v}_2$ x $\vec{v}_3$])

466 The MATLAB class 'msdanalyzer' was used to evaluate mean square displacement
467 (Tarantino et al., 2014).

468

469 **Brightfield motion assay**

470 Sample preparation: Several (>=4) gravid adults per strain were dissected directly in an
471 M9 filled glass bottom microwell imaging dish (MatTek Corp., P35G-1.5-20-C). Up to 60 pre-
472 twitching embryos were arrayed on a patch of poly-L-lysine (0.1 mg/mL) using water currents
473 generated with a worm pick. Worm remains and unwanted embryos were removed with a
474 micropipette and the dish was lidded.

475 Microscope: Embryo arrays were recorded on an inverted microscope (Zeiss, Axiovert
476 100) with a 5x, 0.25 NA objective. A CCD camera (CoolSNAP HQ2) generated 16-bit images with
477 a pixel size of 1.29 μm. Transmitted light power was adjusted to get background pixel counts of
478 ~500 from a 2 ms exposure. Images were acquired at 1 Hz using Micro-Manager control
479 software.

480 Analysis: Pixel intensities were extracted from a box (21x21 pixels) centered on each
481 embryo and frame to frame pixel intensity changes larger than threshold (25) were tallied. The
482 onset of sustained twitching was detected as the first tally (smoothed over 30 frames) greater
483 than X pixels (120 of a potential 441). Background intensity for each frame was also extracted
484 from a perimeter around the embryo (61x61 pixels). Hatching was detected as the point at
485 which the mean intensity at the embryo position (smoothed over 30 frames) approximated the
486 mean intensity of the background perimeter (signal-to-background ratio of at least 0.92). Fresh
487 hatchlings occasionally swam into the field of view, registering pixel changes in the embryo and
488 background perimeter. Data were therefore excluded for frames in which the background
489 perimeter registered changes greater than threshold (35) in more than X pixels (40 of a
490 potential 240 when smoothed over 30 frames).
491 Peak SWT power ratios were computed as follows:
492 1) For each embryo, 15 min twitch profiles were extracted with a sliding window (200 s
493 step size) from 1 h post twitch until hatching. Missing datapoints were replaced with a reversed
494 duplication of the immediately preceding interval of the same length.
495 2) Using MATLAB's Fast Fourier transform ('fft') function, each 15 min twitch profile was
496 transformed from the time domain (i.e. pixels changing per second, $y(t)$) to the frequency
497 domain, $Y(f)$ for equally spaced frequency bins from $f_0 = 0$ to $f_{900} = 1$ Hz, i.e. the sampling rate.
498 3) For each 15 min twitch profile, the proportion of the signal attributed to the SWT
499 frequency band was computed:
500 $$\text{SWT power ratio} = \sum_{0.02 \le f \le 0.04\ \text{Hz}} |Y(f)|^2 \ / \sum_{0 < f \le 0.5\text{Hz}} |Y(f)|^2$$

501 4) For each embryo, the timing and magnitude of the largest SWT power ratio was
502 recorded.
503 To estimate a baseline for peak SWT power ratios (i.e., the dashed lines in Figs. 5e, 6a),
504 pairs of neighbouring values were randomly shuffled prior to the discrete Fourier
505 transformation (between steps 1 and 2 above) for a sample of wild-type embryos.
506 Scalograms were generated using MATLAB's Continuous 1-D wavelet transform ('cwt')
507 function (with 'morse' wavelet).
508 **Calcium imaging**
509 Sample preparation: Several (>=15) gravid adults per strain were dissected directly in an
510 M9 filled glass bottom microwell imaging dish (MatTek Corp., P35G-1.5-20-C). Embryos with no
511 more than 4-cells were selected using currents generated with a worm pick and stuck to a patch
512 of poly-L-lysine (0.1 mg/mL) in pairs, aligned end to end along their major axis (a configuration
513 that enabled imaging two embryos per scan). Worm remains and unwanted embryos were
514 removed with a micropipette and the dish was lidded. Prior to calcium imaging, the brightfield
515 assay (see above) was used to time first twitch.
516 Microscope: At least 215 minutes after the onset of twitching (i.e., ~645 mpf), embryos
517 were imaged on an inverted confocal microscope (Nikon, Eclipse Ti2) using a 20x, 0.75 NA
518 objective. Resonant scanning in two directions generated image planes of 1024x256 pixels (0.16
519 μm/pixel) for two channels (488 and 561 nm lasers) in 33.3 ms. Two embryos were imaged per
520 scan. Volumes were acquired at 1 Hz for 5 min using a piezo stage stepping 7.875 μm between
521 5 image planes (note that the pinhole was opened to minimize the number of steps required to
522 span the embryos).

523 Analysis: RIS cell body position and corresponding GCaMP and mCherry intensity were
524 extracted from an image volume cropped around a single embryo. Specifically, following
525 background subtraction (pixel counts-100), each image plane was filtered using a Gaussian
526 smoothing kernel with standard deviation of 5 (MATLAB's 'imgaussfilt' function with
527 'symmetric' image padding to prevent edge artifacts). The position of the RIS cell body was
528 identified in the mCherry channel as the brightest pixel of the filtered volume. The
529 corresponding intensity in the filtered GCaMP channel was used to compute $\Delta R/R_o = (R - R_o) /$
530 R_o, where R is the GCaMP/mCherry ratio and R_o is the ratio at baseline, set as the 10th
531 percentile for each trace. Calcium transients were identified in smoothed traces (moving mean
532 with span 4) using an onset threshold of $\Delta R/R >= 2$ and an offset threshold of $\Delta R/R < 1.5$.
533

534 **Acknowledgements**

535 We thank the MBL Imaging Center, Whitman Fellows Program, and Neurobiology Course for
536 supporting this project; Daniel Colón-Ramos, Zhirong Bao, Anthony Santella, Pavak Shah, Radu
537 Balan, Hank Eden, Ghadi Salem, Richard Ikegami, Troy McDiarmid, Om Patange, and the Kaplan
538 lab for valuable discussions. This work was funded by an NSF grant to A.L. (DGE-1632976), NIH
539 research grants to J.K. (NS32196 and NS121182), and the intramural research program of the
540 National Institute of Biomedical Imaging and Bioengineering within the NIH. Strains were
541 provided by the CGC (funded by NIH Office of Research Infrastructure Programs - P40
542 OD010440).
543

544 **Author Contributions**

Conceptualization, E.L.A., A.L., J.M.K., H.S.; Methodology, E.L.A., A.L., S.X., S.N., H.S.; Investigation, E.L.A., A.L., S.X., B.J.H., R.C.; Formal analysis, E.L.A., A.L.; Software, E.L.A., A.L., S.X.; Writing – Original Draft, E.L.A., A.L.; Writing – Review & Editing, J.M.K., H.S.; Supervision, J.M.K., H.S.

The NIH and its staff do not endorse or recommend any company, product, or service.

The authors declare no competing interests.

References

Ardiel, E. L., Kumar, A., Marbach, J., Christensen, R., Gupta, R., Duncan, W., Daniels, J. S., Stuurman, N., Colón-Ramos, D., & Shroff, H. (2017). Visualizing Calcium Flux in Freely Moving Nematode Embryos. *Biophysical Journal*, *112*(9), 1975–1983. https://doi.org/10.1016/j.bpj.2017.02.035

Balaban, E., Desco, M., & Vaquero, J.-J. (2012). Waking-like Brain Function in Embryos. *Current Biology*, *22*(10), 852–861. https://doi.org/10.1016/j.cub.2012.03.030

Bao, Z., Murray, J. I., Boyle, T., Ooi, S. L., Sandel, M. J., & Waterston, R. H. (2006). Automated cell lineage tracing in Caenorhabditis elegans. *Proceedings of the National Academy of Sciences of the United States of America*, *103*(8), 2707–2712. https://doi.org/10.1073/pnas.0511111103

Baris Atakan, H., Alkanat, T., Cornaglia, M., Trouillon, R., & Gijs, M. A. M. (2020). Automated phenotyping of Caenorhabditis elegans embryos with a high-throughput-screening microfluidic platform. *Microsystems & Nanoengineering*, *6*(1), 24. https://doi.org/10.1038/s41378-020-0132-8

Barnes, K. M., Fan, L., Moyle, M. W., Brittin, C. A., Xu, Y., Colón-Ramos, D. A., Santella, A., & Bao, Z. (2020). Cadherin preserves cohesion across involuting tissues during C. elegans neurulation. *ELife*, *9*. https://doi.org/10.7554/eLife.58626

Bayer, E. A., Liberatore, K. M., Schneider, J. R., Schlesinger, E., He, Z., Birnbaum, S., & Wightman, B. (2021). Insulin signaling and osmotic stress response regulate arousal and developmental progression of C. elegans at hatching. *Genetics*, *iyab202*. https://doi.org/10.1093/genetics/iyab202

Berman, G. J. (2018). Measuring behavior across scales. *BMC Biology*, *16*(1), 23. https://doi.org/10.1186/s12915-018-0494-7

Brenner, S. (1974). The genetics of Caenorhabditis elegans. *Genetics*, *77*(1), 71–94.

Brown, A. E. X., & de Bivort, B. (2018). Ethology as a physical science. *Nature Physics*, *14*(7), 653–657. https://doi.org/10.1038/s41567-018-0093-0

Carreira-Rosario, A., York, R. A., Choi, M., Doe, C. Q., & Clandinin, T. R. (2021). Mechanosensory input during circuit formation shapes Drosophila motor behavior through patterned spontaneous network activity. *Current Biology*, S096098222101126X. https://doi.org/10.1016/j.cub.2021.08.022

Chen, T.-W., Wardill, T. J., Sun, Y., Pulver, S. R., Renninger, S. L., Baohan, A., Schreiter, E. R., Kerr, R. A., Orger, M. B., Jayaraman, V., Looger, L. L., Svoboda, K., & Kim, D. S. (2013). Ultrasensitive fluorescent proteins for imaging neuronal activity. *Nature*, *499*(7458), 295–300. https://doi.org/10.1038/nature12354

Cho, J. Y., & Sternberg, P. W. (2014). Multilevel Modulation of a Sensory Motor Circuit during C. elegans Sleep and Arousal. *Cell*, *156*(1), 249–260. https://doi.org/10.1016/j.cell.2013.11.036

Choi, S., Chatzigeorgiou, M., Taylor, K. P., Schafer, W. R., & Kaplan, J. M. (2013). Analysis of NPR-1 reveals a circuit mechanism for behavioral quiescence in C. elegans. *Neuron*, *78*(5), 869–880. https://doi.org/10.1016/j.neuron.2013.04.002

Christensen, R. P., Bokinsky, A., Santella, A., Wu, Y., Marquina-Solis, J., Guo, M., Kovacevic, I., Kumar, A., Winter, P. W., Tashakkori, N., McCreedy, E., Liu, H., McAuliffe, M., Mohler,

W., Colón-Ramos, D. A., Bao, Z., & Shroff, H. (2015). Untwisting the Caenorhabditis elegans embryo. *ELife*, *4*, e10070. https://doi.org/10.7554/eLife.10070

Churgin, M. A., Jung, S.-K., Yu, C.-C., Chen, X., Raizen, D. M., & Fang-Yen, C. (2017). Longitudinal imaging of Caenorhabditis elegans in a microfabricated device reveals variation in behavioral decline during aging. *ELife*, *6*, e26652. https://doi.org/10.7554/eLife.26652

Çiçek, Ö., Abdulkadir, A., Lienkamp, S. S., Brox, T., & Ronneberger, O. (2016). 3D U-Net: Learning Dense Volumetric Segmentation from Sparse Annotation. In S. Ourselin, L. Joskowicz, M. R. Sabuncu, G. Unal, & W. Wells (Eds.), *Medical Image Computing and Computer-Assisted Intervention – MICCAI 2016* (pp. 424–432). Springer International Publishing. https://doi.org/10.1007/978-3-319-46723-8_49

Cirelli, C. (2006). Cellular consequences of sleep deprivation in the brain. *Sleep Medicine Reviews*, *10*(5), 307–321. https://doi.org/10.1016/j.smrv.2006.04.001

Cook, S. J., Jarrell, T. A., Brittin, C. A., Wang, Y., Bloniarz, A. E., Yakovlev, M. A., Nguyen, K. C. Q., Tang, L. T.-H., Bayer, E. A., Duerr, J. S., Bülow, H. E., Hobert, O., Hall, D. H., & Emmons, S. W. (2019). Whole-animal connectomes of both Caenorhabditis elegans sexes. *Nature*, *571*(7763), 63–71. https://doi.org/10.1038/s41586-019-1352-7

Corner, M. A. (1977). Sleep and the beginnings of behavior in the animal kingdom—Studies of ultradian motility cycles in early life. *Progress in Neurobiology*, *8*(4), 279–295. https://doi.org/10.1016/0301-0082(77)90008-9

Cox, I. J., & Hingorani, S. L. (1996). An efficient implementation of Reid's multiple hypothesis tracking algorithm and its evaluation for the purpose of visual tracking. *IEEE*

Transactions on Pattern Analysis and Machine Intelligence, *18*(2), 138–150. https://doi.org/10.1109/34.481539

Crisp, S. J., Evers, J. F., & Bate, M. (2011). Endogenous patterns of activity are required for the maturation of a motor network. *The Journal of Neuroscience: The Official Journal of the Society for Neuroscience*, *31*(29), 10445–10450. https://doi.org/10.1523/JNEUROSCI.0346-11.2011

Datta, S. R., Anderson, D. J., Branson, K., Perona, P., & Leifer, A. (2019). Computational Neuroethology: A Call to Action. *Neuron*, *104*(1), 11–24. https://doi.org/10.1016/j.neuron.2019.09.038

Duncan, L. H., Moyle, M. W., Shao, L., Sengupta, T., Ikegami, R., Kumar, A., Guo, M., Christensen, R., Santella, A., Bao, Z., Shroff, H., Mohler, W., & Colón-Ramos, D. A. (2019). Isotropic Light-Sheet Microscopy and Automated Cell Lineage Analyses to Catalogue Caenorhabditis elegans Embryogenesis with Subcellular Resolution. *Journal of Visualized Experiments: JoVE*, *148*. https://doi.org/10.3791/59533

Fan, L., Kovacevic, I., Heiman, M. G., & Bao, Z. (2019). A multicellular rosette-mediated collective dendrite extension. *ELife*, *8*. https://doi.org/10.7554/eLife.38065

Frøkjær-Jensen, C., Davis, M. W., Sarov, M., Taylor, J., Flibotte, S., LaBella, M., Pozniakovsky, A., Moerman, D. G., & Jorgensen, E. M. (2014). Random and targeted transgene insertion in Caenorhabditis elegans using a modified Mos1 transposon. *Nature Methods*, *11*(5), 529–534. https://doi.org/10.1038/nmeth.2889

Giurumescu, C. A., Kang, S., Planchon, T. A., Betzig, E., Bloomekatz, J., Yelon, D., Cosman, P., & Chisholm, A. D. (2012). Quantitative semi-automated analysis of morphogenesis with

single-cell resolution in complex embryos. *Development (Cambridge, England)*, *139*(22), 4271–4279. https://doi.org/10.1242/dev.086256

Gonzales, D. L., Zhou, J., Fan, B., & Robinson, J. T. (2019). A microfluidic-induced C. elegans sleep state. *Nature Communications*, *10*(1), 5035. https://doi.org/10.1038/s41467-019-13008-5

Guo, M., Li, Y., Su, Y., Lambert, T., Nogare, D. D., Moyle, M. W., Duncan, L. H., Ikegami, R., Santella, A., Rey-Suarez, I., Green, D., Beiriger, A., Chen, J., Vishwasrao, H., Ganesan, S., Prince, V., Waters, J. C., Annunziata, C. M., Hafner, M., … Shroff, H. (2020). Rapid image deconvolution and multiview fusion for optical microscopy. *Nature Biotechnology*, *38*(11), 1337–1346. https://doi.org/10.1038/s41587-020-0560-x

Hall, D. H., & Hedgecock, E. M. (1991). Kinesin-related gene unc-104 is required for axonal transport of synaptic vesicles in C. elegans. *Cell*, *65*(5), 837–847. https://doi.org/10.1016/0092-8674(91)90391-B

Hallam, S. J., & Jin, Y. (1998). Lin-14 regulates the timing of synaptic remodelling in Caenorhabditis elegans. *Nature*, *395*(6697), 78–82. https://doi.org/10.1038/25757

Hamburger, V. (1963). Some Aspects of the Embryology of Behavior. *The Quarterly Review of Biology*, *38*(4), 342–365. https://doi.org/10.1086/403941

Hardin, P. E., Hall, J. C., & Rosbash, M. (1990). Feedback of the Drosophila period gene product on circadian cycling of its messenger RNA levels. *Nature*, *343*(6258), 536–540. https://doi.org/10.1038/343536a0

Heiman, M. G., & Shaham, S. (2009). DEX-1 and DYF-7 Establish Sensory Dendrite Length by Anchoring Dendritic Tips during Cell Migration. *Cell*, *137*(2), 344–355. https://doi.org/10.1016/j.cell.2009.01.057

Hensch, T. K. (2004). CRITICAL PERIOD REGULATION. *Annual Review of Neuroscience*, *27*(1), 549–579. https://doi.org/10.1146/annurev.neuro.27.070203.144327

Hill, A. J., Mansfield, R., Lopez, J. M. N. G., Raizen, D. M., & Van Buskirk, C. (2014). Cellular stress induces a protective sleep-like state in C. elegans. *Current Biology: CB*, *24*(20), 2399–2405. https://doi.org/10.1016/j.cub.2014.08.040

Hong, M., Ryu, L., Ow, M. C., Kim, J., Je, A. R., Chinta, S., Huh, Y. H., Lee, K. J., Butcher, R. A., Choi, H., Sengupta, P., Hall, S. E., & Kim, K. (2017). Early Pheromone Experience Modifies a Synaptic Activity to Influence Adult Pheromone Responses of C. elegans. *Current Biology: CB*, *27*(20), 3168-3177.e3. https://doi.org/10.1016/j.cub.2017.08.068

Hu, Y., Korovaichuk, A., Astiz, M., Schroeder, H., Islam, R., Barrenetxea, J., Fischer, A., Oster, H., & Bringmann, H. (2020). Functional Divergence of Mammalian TFAP2a and TFAP2b Transcription Factors for Bidirectional Sleep Control. *Genetics*, *216*(3), 735–752. https://doi.org/10.1534/genetics.120.303533

Iwanir, S., Tramm, N., Nagy, S., Wright, C., Ish, D., & Biron, D. (2013). The microarchitecture of C. elegans behavior during lethargus: Homeostatic bout dynamics, a typical body posture, and regulation by a central neuron. *Sleep*, *36*(3), 385–395. https://doi.org/10.5665/sleep.2456

Kirkby, L. A., Sack, G. S., Firl, A., & Feller, M. B. (2013). A role for correlated spontaneous activity in the assembly of neural circuits. *Neuron*, *80*(5), 1129–1144. https://doi.org/10.1016/j.neuron.2013.10.030

Konopka, R. J., & Benzer, S. (1971). Clock mutants of Drosophila melanogaster. *Proceedings of the National Academy of Sciences of the United States of America*, *68*(9), 2112–2116. https://doi.org/10.1073/pnas.68.9.2112

Kucherenko, M. M., Ilangovan, V., Herzig, B., Shcherbata, H. R., & Bringmann, H. (2016). TfAP-2 is required for night sleep in Drosophila. *BMC Neuroscience*, *17*(1), 72. https://doi.org/10.1186/s12868-016-0306-3

Kumar, A., Christensen, R., Guo, M., Chandris, P., Duncan, W., Wu, Y., Santella, A., Moyle, M., Winter, P. W., Colón-Ramos, D., Bao, Z., & Shroff, H. (2016). Using Stage- and Slit-Scanning to Improve Contrast and Optical Sectioning in Dual-View Inverted Light Sheet Microscopy (diSPIM). *The Biological Bulletin*, *231*(1), 26–39. https://doi.org/10.1086/689589

Kumar, A., Wu, Y., Christensen, R., Chandris, P., Gandler, W., McCreedy, E., Bokinsky, A., Colón-Ramos, D. A., Bao, Z., McAuliffe, M., Rondeau, G., & Shroff, H. (2014). Dual-view plane illumination microscopy for rapid and spatially isotropic imaging. *Nature Protocols*, *9*(11), 2555–2573. https://doi.org/10.1038/nprot.2014.172

Mani, A., Radhakrishnan, J., Farhi, A., Carew, K. S., Warnes, C. A., Nelson-Williams, C., Day, R. W., Pober, B., State, M. W., & Lifton, R. P. (2005). Syndromic patent ductus arteriosus: Evidence for haploinsufficient TFAP2B mutations and identification of a linked sleep

disorder. *Proceedings of the National Academy of Sciences of the United States of America*, *102*(8), 2975–2979. https://doi.org/10.1073/pnas.0409852102

McDonald, N. A., Fetter, R. D., & Shen, K. (2020). Assembly of synaptic active zones requires phase separation of scaffold molecules. *Nature*, *588*(7838), 454–458. https://doi.org/10.1038/s41586-020-2942-0

Meeuse, M. W., Hauser, Y. P., Morales Moya, L. J., Hendriks, G.-J., Eglinger, J., Bogaarts, G., Tsiairis, C., & Großhans, H. (2020). Developmental function and state transitions of a gene expression oscillator in Caenorhabditis elegans. *Molecular Systems Biology*, *16*(7), e9498. https://doi.org/10.15252/msb.20209498

Monsalve, G. C., Van Buskirk, C., & Frand, A. R. (2011). LIN-42/PERIOD controls cyclical and developmental progression of C. elegans molts. *Current Biology: CB*, *21*(24), 2033–2045. https://doi.org/10.1016/j.cub.2011.10.054

Moyle, M. W., Barnes, K. M., Kuchroo, M., Gonopolskiy, A., Duncan, L. H., Sengupta, T., Shao, L., Guo, M., Santella, A., Christensen, R., Kumar, A., Wu, Y., Moon, K. R., Wolf, G., Krishnaswamy, S., Bao, Z., Shroff, H., Mohler, W. A., & Colón-Ramos, D. A. (2021). Structural and developmental principles of neuropil assembly in C. elegans. *Nature*, *591*(7848), 99–104. https://doi.org/10.1038/s41586-020-03169-5

Nagy, S., Tramm, N., Sanders, J., Iwanir, S., Shirley, I. A., Levine, E., & Biron, D. (2014). Homeostasis in C. elegans sleep is characterized by two behaviorally and genetically distinct mechanisms. *ELife*, *3*, e04380. https://doi.org/10.7554/eLife.04380

Naidoo, N., Giang, W., Galante, R. J., & Pack, A. I. (2005). Sleep deprivation induces the unfolded protein response in mouse cerebral cortex. *Journal of Neurochemistry*, *92*(5), 1150–1157. https://doi.org/10.1111/j.1471-4159.2004.02952.x

Nath, R. D., Chow, E. S., Wang, H., Schwarz, E. M., & Sternberg, P. W. (2016). C. elegans Stress-Induced Sleep Emerges from the Collective Action of Multiple Neuropeptides. *Current Biology: CB*, *26*(18), 2446–2455. https://doi.org/10.1016/j.cub.2016.07.048

Okai, T., Kozuma, S., Shinozuka, N., Kuwabara, Y., & Mizuno, M. (1992). A study on the development of sleep-wakefulness cycle in the human fetus. *Early Human Development*, *29*(1–3), 391–396. https://doi.org/10.1016/0378-3782(92)90198-p

Packer, J. S., Zhu, Q., Huynh, C., Sivaramakrishnan, P., Preston, E., Dueck, H., Stefanik, D., Tan, K., Trapnell, C., Kim, J., Waterston, R. H., & Murray, J. I. (2019). A lineage-resolved molecular atlas of C. elegans embryogenesis at single-cell resolution. *Science (New York, N.Y.)*, *365*(6459), eaax1971. https://doi.org/10.1126/science.aax1971

Parikshak, N. N., Luo, R., Zhang, A., Won, H., Lowe, J. K., Chandran, V., Horvath, S., & Geschwind, D. H. (2013). Integrative Functional Genomic Analyses Implicate Specific Molecular Pathways and Circuits in Autism. *Cell*, *155*(5), 1008–1021. https://doi.org/10.1016/j.cell.2013.10.031

Pereanu, W., Spindler, S., Im, E., Buu, N., & Hartenstein, V. (2007). The emergence of patterned movement during late embryogenesis of Drosophila. *Developmental Neurobiology*, *67*(12), 1669–1685. https://doi.org/10.1002/dneu.20538

Pereira, T. D., Shaevitz, J. W., & Murthy, M. (2020). Quantifying behavior to understand the brain. *Nature Neuroscience*, *23*(12), 1537–1549. https://doi.org/10.1038/s41593-020-00734-z

Preyer, W. T. (1885). *Specielle Physiologie des Embryo: Untersuchungen ueber die Lebenserscheinungen vor der Geburt*. Th. Grieben's Verlag (L. Fernau).

Priess, J. R., & Hirsh, D. I. (1986). Caenorhabditis elegans morphogenesis: The role of the cytoskeleton in elongation of the embryo. *Developmental Biology*, *117*(1), 156–173. https://doi.org/10.1016/0012-1606(86)90358-1

Pujol, N., Torregrossa, P., Ewbank, J. J., & Brunet, J. F. (2000). The homeodomain protein CePHOX2/CEH-17 controls antero-posterior axonal growth in C. elegans. *Development (Cambridge, England)*, *127*(15), 3361–3371.

Raizen, D. M., Zimmerman, J. E., Maycock, M. H., Ta, U. D., You, Y., Sundaram, M. V., & Pack, A. I. (2008). Lethargus is a Caenorhabditis elegans sleep-like state. *Nature*, *451*(7178), 569–572. https://doi.org/10.1038/nature06535

Reid, D. (1979). An algorithm for tracking multiple targets. *IEEE Transactions on Automatic Control*, *24*(6), 843–854. https://doi.org/10.1109/TAC.1979.1102177

Richard Durbin Thesis 1987 Part I. (n.d.). Retrieved October 8, 2021, from https://www.wormatlas.org/Durbin/Durbin1987partI.html

Richmond, J. E., Davis, W. S., & Jorgensen, E. M. (1999). UNC-13 is required for synaptic vesicle fusion in C. elegans. *Nature Neuroscience*, *2*(11), 959–964. https://doi.org/10.1038/14755

Richmond, J. E., & Jorgensen, E. M. (1999). One GABA and two acetylcholine receptors function at the C. elegans neuromuscular junction. *Nature Neuroscience*, *2*(9), 791–797. https://doi.org/10.1038/12160

Sanders, J., Scholz, M., Merutka, I., & Biron, D. (2017). Distinct unfolded protein responses mitigate or mediate effects of nonlethal deprivation of C. elegans sleep in different tissues. *BMC Biology*, *15*(1), 67. https://doi.org/10.1186/s12915-017-0407-1

Satterstrom, F. K., Kosmicki, J. A., Wang, J., Breen, M. S., De Rubeis, S., An, J.-Y., Peng, M., Collins, R., Grove, J., Klei, L., Stevens, C., Reichert, J., Mulhern, M. S., Artomov, M., Gerges, S., Sheppard, B., Xu, X., Bhaduri, A., Norman, U., … Walters, R. K. (2020). Large-Scale Exome Sequencing Study Implicates Both Developmental and Functional Changes in the Neurobiology of Autism. *Cell*, *180*(3), 568-584.e23. https://doi.org/10.1016/j.cell.2019.12.036

Schwarz, J., & Bringmann, H. (2017). Analysis of the NK2 homeobox gene ceh-24 reveals sublateral motor neuron control of left-right turning during sleep. *ELife*, *6*, e24846. https://doi.org/10.7554/eLife.24846

Sengupta, T., Koonce, N. L., Moyle, M. W., Duncan, L. H., Vázquez-Martínez, N., Emerson, S. E., Han, X., Shao, L., Wu, Y., Santella, A., Fan, L., Bao, Z., Mohler, W. A., Shroff, H., & Colón-Ramos, D. A. (2021). *Differential adhesion regulates neurite placement via a retrograde zippering mechanism* (p. 2020.08.28.271437). https://www.biorxiv.org/content/10.1101/2020.08.28.271437v2

Shah, P. K., Tanner, M. R., Kovacevic, I., Rankin, A., Marshall, T. E., Noblett, N., Tran, N. N., Roenspies, T., Hung, J., Chen, Z., Slatculescu, C., Perkins, T. J., Bao, Z., & Colavita, A.

(2017). PCP and SAX-3/Robo Pathways Cooperate to Regulate Convergent Extension-Based Nerve Cord Assembly in C. elegans. *Developmental Cell*, *41*(2), 195-203.e3. https://doi.org/10.1016/j.devcel.2017.03.024

Shaw, P. J., Cirelli, C., Greenspan, R. J., & Tononi, G. (2000). Correlates of sleep and waking in Drosophila melanogaster. *Science (New York, N.Y.)*, *287*(5459), 1834–1837. https://doi.org/10.1126/science.287.5459.1834

Skora, S., Mende, F., & Zimmer, M. (2018). Energy Scarcity Promotes a Brain-wide Sleep State Modulated by Insulin Signaling in C. elegans. *Cell Reports*, *22*(4), 953–966. https://doi.org/10.1016/j.celrep.2017.12.091

Stern, S., Kirst, C., & Bargmann, C. I. (2017). Neuromodulatory Control of Long-Term Behavioral Patterns and Individuality across Development. *Cell*, *171*(7), 1649-1662.e10. https://doi.org/10.1016/j.cell.2017.10.041

Sun, Z. S., Albrecht, U., Zhuchenko, O., Bailey, J., Eichele, G., & Lee, C. C. (1997). RIGUI, a putative mammalian ortholog of the Drosophila period gene. *Cell*, *90*(6), 1003–1011. https://doi.org/10.1016/s0092-8674(00)80366-9

Szeto, H. H., & Hinman, D. J. (1985). Prenatal development of sleep-wake patterns in sheep. *Sleep*, *8*(4), 347–355. https://doi.org/10.1093/sleep/8.4.347

Tarantino, N., Tinevez, J.-Y., Crowell, E. F., Boisson, B., Henriques, R., Mhlanga, M., Agou, F., Israël, A., & Laplantine, E. (2014). TNF and IL-1 exhibit distinct ubiquitin requirements for inducing NEMO–IKK supramolecular structures. *Journal of Cell Biology*, *204*(2), 231–245. https://doi.org/10.1083/jcb.201307172

Tei, H., Okamura, H., Shigeyoshi, Y., Fukuhara, C., Ozawa, R., Hirose, M., & Sakaki, Y. (1997). Circadian oscillation of a mammalian homologue of the Drosophila period gene. *Nature*, *389*(6650), 512–516. https://doi.org/10.1038/39086

Terao, A., Steininger, T. L., Hyder, K., Apte-Deshpande, A., Ding, J., Rishipathak, D., Davis, R. W., Heller, H. C., & Kilduff, T. S. (2003). Differential increase in the expression of heat shock protein family members during sleep deprivation and during sleep. *Neuroscience*, *116*(1), 187–200. https://doi.org/10.1016/s0306-4522(02)00695-4

Touroutine, D., Fox, R. M., Von Stetina, S. E., Burdina, A., Miller, D. M., & Richmond, J. E. (2005). Acr-16 encodes an essential subunit of the levamisole-resistant nicotinic receptor at the Caenorhabditis elegans neuromuscular junction. *The Journal of Biological Chemistry*, *280*(29), 27013–27021. https://doi.org/10.1074/jbc.M502818200

Tramm, N., Oppenheimer, N., Nagy, S., Efrati, E., & Biron, D. (2014). Why do sleeping nematodes adopt a hockey-stick-like posture? *PloS One*, *9*(7), e101162. https://doi.org/10.1371/journal.pone.0101162

Turek, M., Besseling, J., Spies, J.-P., König, S., & Bringmann, H. (2016). Sleep-active neuron specification and sleep induction require FLP-11 neuropeptides to systemically induce sleep. *ELife*, *5*. https://doi.org/10.7554/eLife.12499

Turek, M., Lewandrowski, I., & Bringmann, H. (2013). An AP2 transcription factor is required for a sleep-active neuron to induce sleep-like quiescence in C. elegans. *Current Biology: CB*, *23*(22), 2215–2223. https://doi.org/10.1016/j.cub.2013.09.028

Van Buskirk, C., & Sternberg, P. W. (2007). Epidermal growth factor signaling induces behavioral quiescence in Caenorhabditis elegans. *Nature Neuroscience*, *10*(10), 1300–1307. https://doi.org/10.1038/nn1981

White, J. G., Albertson, D. G., & Anness, M. A. (1978). Connectivity changes in a class of motoneurone during the development of a nematode. *Nature*, *271*(5647), 764–766. https://doi.org/10.1038/271764a0

White, J. G., Southgate, E., Thomson, J. N., & Brenner, S. (1986). The structure of the nervous system of the nematode Caenorhabditis elegans. *Philosophical Transactions of the Royal Society of London. Series B, Biological Sciences*, *314*(1165), 1–340.

Williams, B. D., & Waterston, R. H. (1994). Genes critical for muscle development and function in Caenorhabditis elegans identified through lethal mutations. *The Journal of Cell Biology*, *124*(4), 475–490. https://doi.org/10.1083/jcb.124.4.475

Willsey, A. J., Sanders, S. J., Li, M., Dong, S., Tebbenkamp, A. T., Muhle, R. A., Reilly, S. K., Lin, L., Fertuzinhos, S., Miller, J. A., Murtha, M. T., Bichsel, C., Niu, W., Cotney, J., Ercan-Sencicek, A. G., Gockley, J., Gupta, A. R., Han, W., He, X., … State, M. W. (2013). Coexpression Networks Implicate Human Midfetal Deep Cortical Projection Neurons in the Pathogenesis of Autism. *Cell*, *155*(5), 997–1007. https://doi.org/10.1016/j.cell.2013.10.020

Wintler, T., Schoch, H., Frank, M. G., & Peixoto, L. (2020). Sleep, brain development, and autism spectrum disorders: Insights from animal models. *Journal of Neuroscience Research*, *98*(6), 1137–1149. https://doi.org/10.1002/jnr.24619

Witvliet, D., Mulcahy, B., Mitchell, J. K., Meirovitch, Y., Berger, D. R., Wu, Y., Liu, Y., Koh, W. X., Parvathala, R., Holmyard, D., Schalek, R. L., Shavit, N., Chisholm, A. D., Lichtman, J. W., Samuel, A. D. T., & Zhen, M. (2021). Connectomes across development reveal principles of brain maturation. *Nature*, *596*(7871), 257–261. https://doi.org/10.1038/s41586-021-03778-8

Wu, Y., Masurat, F., Preis, J., & Bringmann, H. (2018). Sleep Counteracts Aging Phenotypes to Survive Starvation-Induced Developmental Arrest in C. elegans. *Current Biology: CB*, *28*(22), 3610-3624.e8. https://doi.org/10.1016/j.cub.2018.10.009

Wu, Y., Wawrzusin, P., Senseney, J., Fischer, R. S., Christensen, R., Santella, A., York, A. G., Winter, P. W., Waterman, C. M., Bao, Z., Colón-Ramos, D. A., McAuliffe, M., & Shroff, H. (2013). Spatially isotropic four-dimensional imaging with dual-view plane illumination microscopy. *Nature Biotechnology*, *31*(11), 1032–1038. https://doi.org/10.1038/nbt.2713

You, Y., Kim, J., Raizen, D. M., & Avery, L. (2008). Insulin, cGMP, and TGF-beta signals regulate food intake and quiescence in C. elegans: A model for satiety. *Cell Metabolism*, *7*(3), 249–257. https://doi.org/10.1016/j.cmet.2008.01.005

Fig. 1. Tracking seams cells with Multiple Hypothesis Hypergraph Tracking (MHHT). a) Embryonic timeline with imaging window highlighted. mpf: minutes post fertilization. b) XY maximum intensity projection of an embryo expressing GFP in hypodermal seam cell nuclei (left). Segmented (center) and identified seam cells (right). MHHT: Multiple Hypothesis Hypergraph Tracking. Scale bar, 10 μm. c) Frame-to-frame displacement of V2 along the x-axis of the image correlates with that of other seam cells (top). Frame-to-frame change in the distance between V2 and V3 correlates with neighbouring edge length changes (bottom). See Supp. Fig. S1 for full correlation matrices. d) A cell assignment search tree with width *K*=2 and depth *N*=3. Physically impossible body contortions (self-intersections) are pruned (scissors). The path accruing the least cost is highlighted (outlined circles).

Fig 2. Eigen-embryos compactly describe behavioral maturation. a) Schematic depicting the definition of a dorsoventral (DV) bend. Top: Adjacent seam cell nuclei positions (colored balls) are fit with a natural cubic spline (black line), open circles denote the midpoint between seam cell nuclei. Bottom: View looking down $\vec{v}_2$ to highlight a dorsal DV bend on one side of the body. Curved red arrow indicates DV bend angle. b) DV bends along the left and right sides of the body ('+' and 'o'; top), with the corresponding posture model (bottom). Seam cell nuclei are fit with a natural cubic spline from H0 (blue) to tail (yellow). c) Fraction of the total variance captured by reconstructing postures using 1 through all 18 principal components. d) Fraction of the total variance captured by the first 4 principal components as a function of age. e) Eigen-embryos, i.e. eigenvectors for the first 4 PCs, derived from the 3 individual embryos in grey and from pooled datasets in color. Right: sample postures drawn from the 95th percentile of

amplitudes for the corresponding PC. f) An embryo's PC1 amplitude from 530 mpf until hatch (top). DV bend profiles over highlighted 20 min windows with corresponding PC2 and PC3 amplitudes (bottom).

Fig 3. Transition to punctuated and directed movement ahead of hatching. a) Mean square displacement (MSD) for each seam cell nucleus of an embryo, 530 to 770 mpf. Dotted line depicts predicted unconfined Brownian motion for the H1 seam cell. b) Mean diffusion coefficient (D) for each seam cell pair. X-axis label colored as in a). Three individual embryos in grey, mean +/- SEM in black. c) Diffusion coefficients for all cells computed over 20 min bins. Individual embryos in grey, mean +/- SEM in black. d) Tracks of an H1 and V6 seam cell over 20 minutes at indicated age (left). Darker tracks indicate larger movements ('v'), color-code shows direction of motion along the anteroposterior axis ('θ'; see schematic representation of 'v' and 'θ' at right). e) Embryo speed on a log-scale to highlight late stage pausing (top). Higher magnification views over highlighted 5 min intervals (bottom), with labels for the direction of motion and pausing (pauses defined as embryo speed < 0.5 μm/s). f) Coefficient of variation in embryo speed for 20 min bins. Individual embryos in grey, mean +/- SEM in black. g) Mean duration of forward, backward, and pausing bouts for 20 min bins. Individual embryos are represented as fainter lines with mean +/- SEM in bold.

Fig 4. *unc-13* mutants have a late-stage motility defect. a) 10 min tracks of an H1 seam cell (left) and mean diffusion coefficients of seam cell pairs (right; mean +/- SEM) at 750 mpf for control (WT, n=3) and *unc-13* mutants (n=3). Scale bar, 10 μm. b) Same as a) for 530 mpf (WT,

n=3; *unc-13*, n=2). c) Duration of transitions between fully dorsally and fully ventrally coiled postures from 530-540 mpf. d) An embryo's transitions from ventral to dorsal coiling through posture space from 530-540 mpf (note that only transitions executed in <=10 seconds are plotted). Flips were categorized into four motifs based on the mean amplitude of PC2 and PC3 during the transition (PC2+, PC2-, PC3+, and PC3-). Arrowheads and dots denote the start and end of the flip, respectively, i.e., the last fully ventrally coiled posture to the first fully dorsally coiled posture. e) Summary of coiling transition trajectories in posture space at 530 mpf, with arrowhead sizes indicating the frequency of occurrence. Color-code matches d). Schematized worms are shown as black squiggles with ventral side down and red dot at head.

Fig. 5. A brightfield assay for screening mutants reveals the 'slow wave twitch' (SWT) as a behavioral signature dependent on cholinergic and peptidergic signalling. a) 30 embryos arrayed for the brightfield assay (left). Scale bar, 100 μm. Zoomed images (scale bar, 10 μm) over 3 consecutive frames of the embryo highlighted in the array, with difference images shown below (right). Sample trace depicts the proportion of pixels changing at twitch onset. b) Brightfield assay summary for wild-type (WT; n = 24) and *unc-13* mutants (n = 23), with each line corresponding to an embryo aligned at twitch onset and color-coded by the proportion of pixels changing intensity (smoothed over 10s). c) Difference between wild-type and *unc-13* mutant scalograms (see Supp. Fig. S3b for mean scalograms). Note that the feature in the 20-40 mHz frequency band at ~660 to 720 mpf (arrow) represents the 'slow wave twitch' (SWT). d) Timing of peak relative power in the SWT frequency band (20-40 mHz). Mean +/- SEM, with each dot corresponding to an embryo. e) Peak relative power in the SWT frequency band in

several synaptic signalling mutants. Mean +/- SEM, with each dot corresponding to an embryo. One-way ANOVA and Tukey's honestly significant difference criterion were used to compare strains. Asterisks denote strains statistically distinguishable from wild-type at $p < 0.001$. The dashed line shows the average peak SWT power ratio derived from shuffled wild-type data.

Fig. 6. SWT is mediated by FLP-11 neuropeptides released from RIS. a) Left: Proportion of pixels changing during the 15 min window over which the SWT power ratio peaked. Right: Peak relative power in the SWT frequency band (20-40 mHz). Mean +/- SEM, with each dot corresponding to an embryo. The dashed line denotes the average peak SWT power ratio derived from shuffled data. Alleles for *aptf-1* refer to *gk794* and *tm3287*. b) Top: Brightfield assay summary for wild-type (WT) and *flp-11* mutants, with each line corresponding to an embryo aligned at twitch onset and color-coded by the proportion of pixels changing intensity (smoothed over 10s). Bottom: Wild-type and *flp-11* scalograms. Note the SWT signature in WT (arrow) is missing in *flp-11*. c) A single slice from an image volume of an embryo expressing GCaMP (top) fused to mCherry (bottom) in RIS. Time stamp in seconds and scale bar, 10 μm. d) Representative traces of RIS movement (above) and activity (below), as measured by normalized GCaMP/mCherry ratios at the cell body. Grey bands denote calcium transient width at half max. Green bar spans the period depicted in c). e) Frequency of calcium transients and quiescent bouts (quiescence defined as speed <= 0.5 μm/s for at least 3 s). f) Duration of calcium transients (peak width at half max) and quiescent bouts. Mean +/- SEM, with each dot corresponding to an embryo. One-way ANOVA and Tukey's honestly significant difference

criterion were used to compare strains. Asterisks denote statistically distinguishable groups at $p < 0.001$. g) Cross correlation between fluorophore intensity and RIS speed.

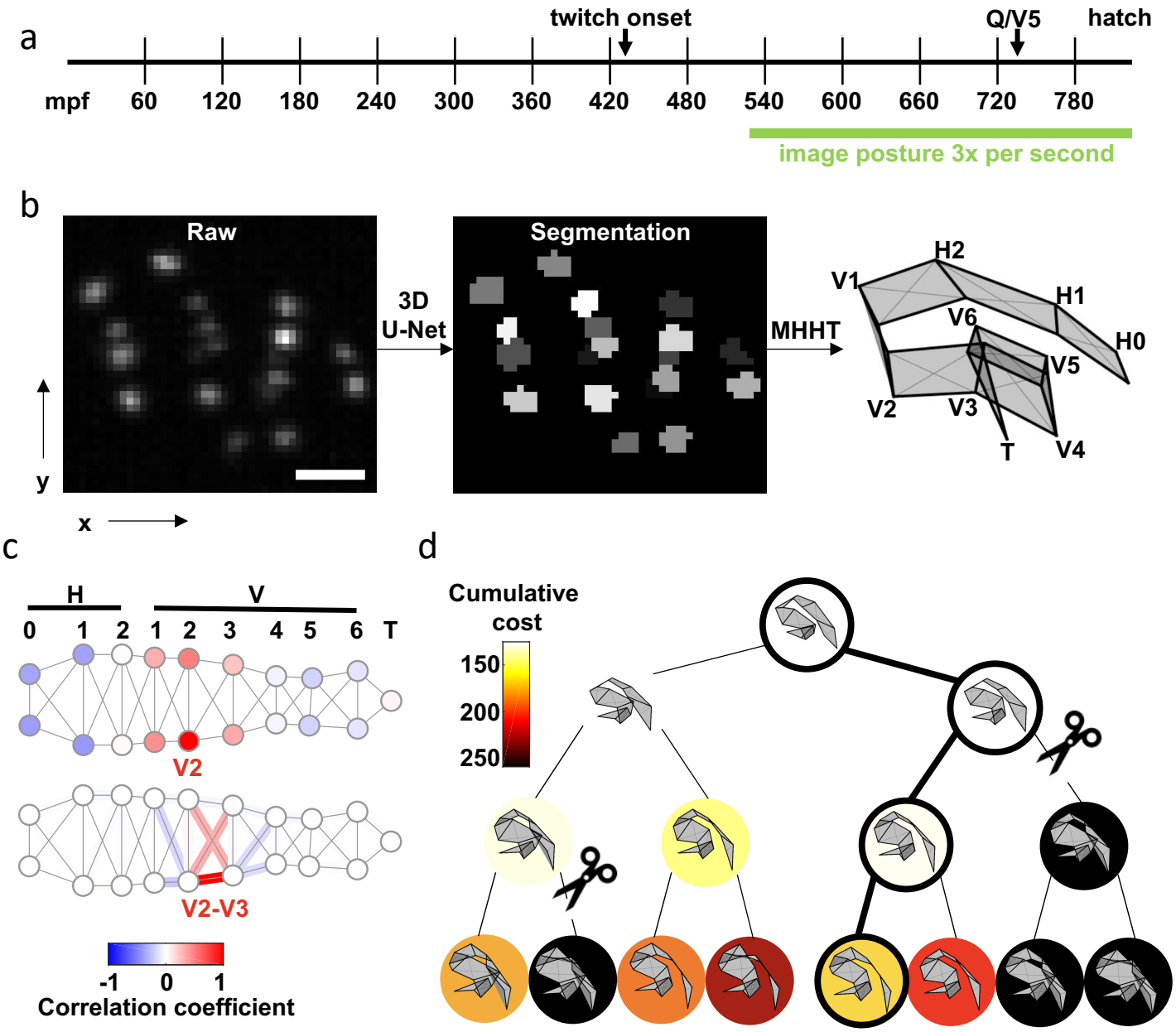
a
twitch onset
Q/V5
hatch
mpf
60
120
180
240
300
360
420
480
540
600
660
720
780
image posture 3x per second
b
Raw
3D
U-Net
Segmentation
MHHT
H2
V1
H1
V6
H0
V5
V2
V3
T
V4
y
x
c
H
V
0
1
2
1
2
3
4
5
6
T
V2
V2-V3
-1
0
1
Correlation coefficient
d
Cumulative
cost
150
200
250

Fig. 1.

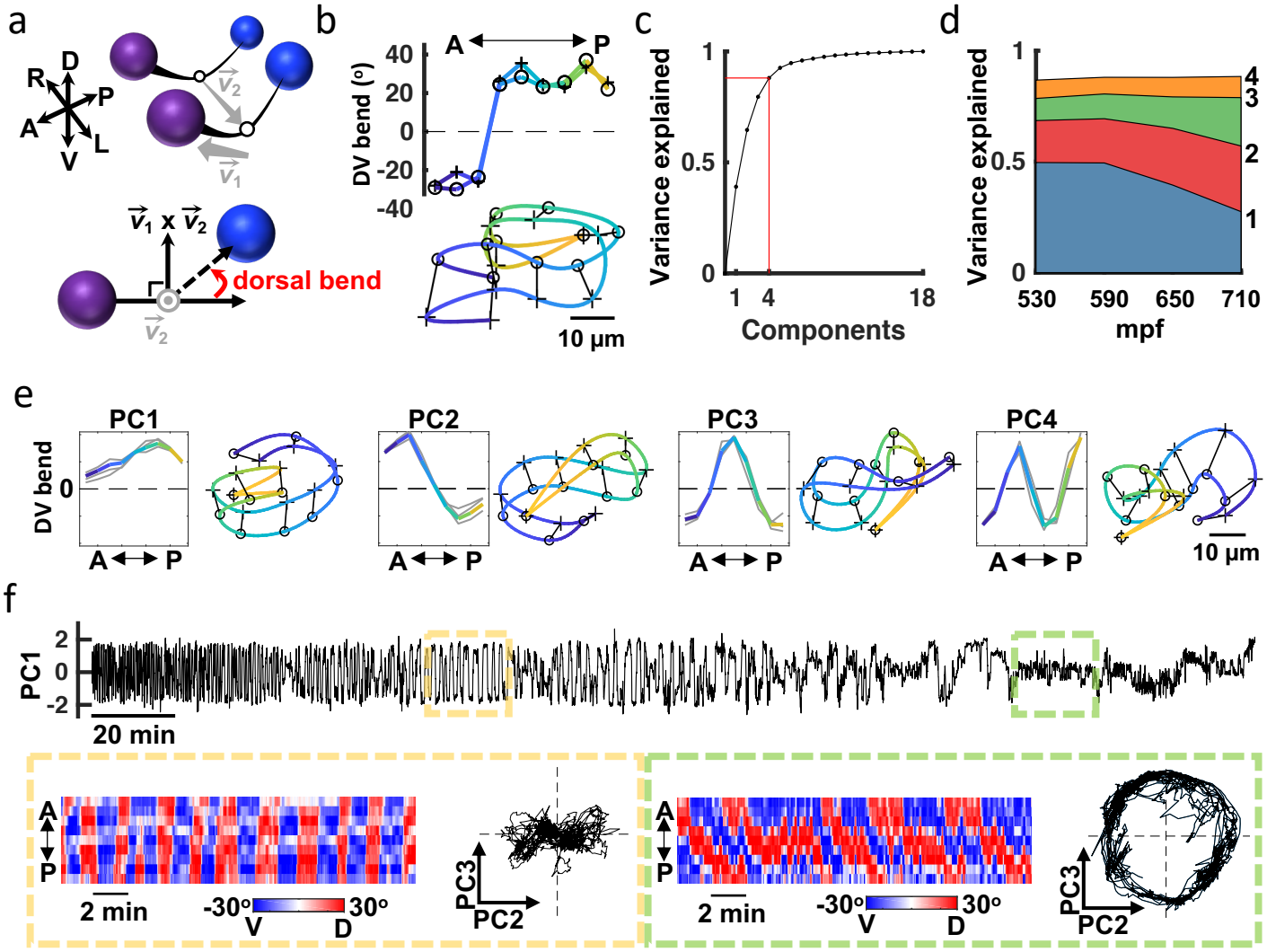
a
D
R
P
A
L
V
$\vec{v}_2$
$\vec{v}_1$
$\vec{v}_1$ x $\vec{v}_2$
dorsal bend
$\vec{v}_2$
b
A
P
DV bend (°)
40
20
0
-20
-40
10 µm
c
Variance explained
1
0.5
0
1
4
18
Components
d
Variance explained
1
0.5
0
530
590
650
710
mpf
4
3
2
1
e
PC1
PC2
PC3
PC4
DV bend
0
A
P
10 µm
f
PC1
2
0
-2
20 min
A
P
2 min
-30°
30°
V
D
PC3
PC2

Fig. 2.

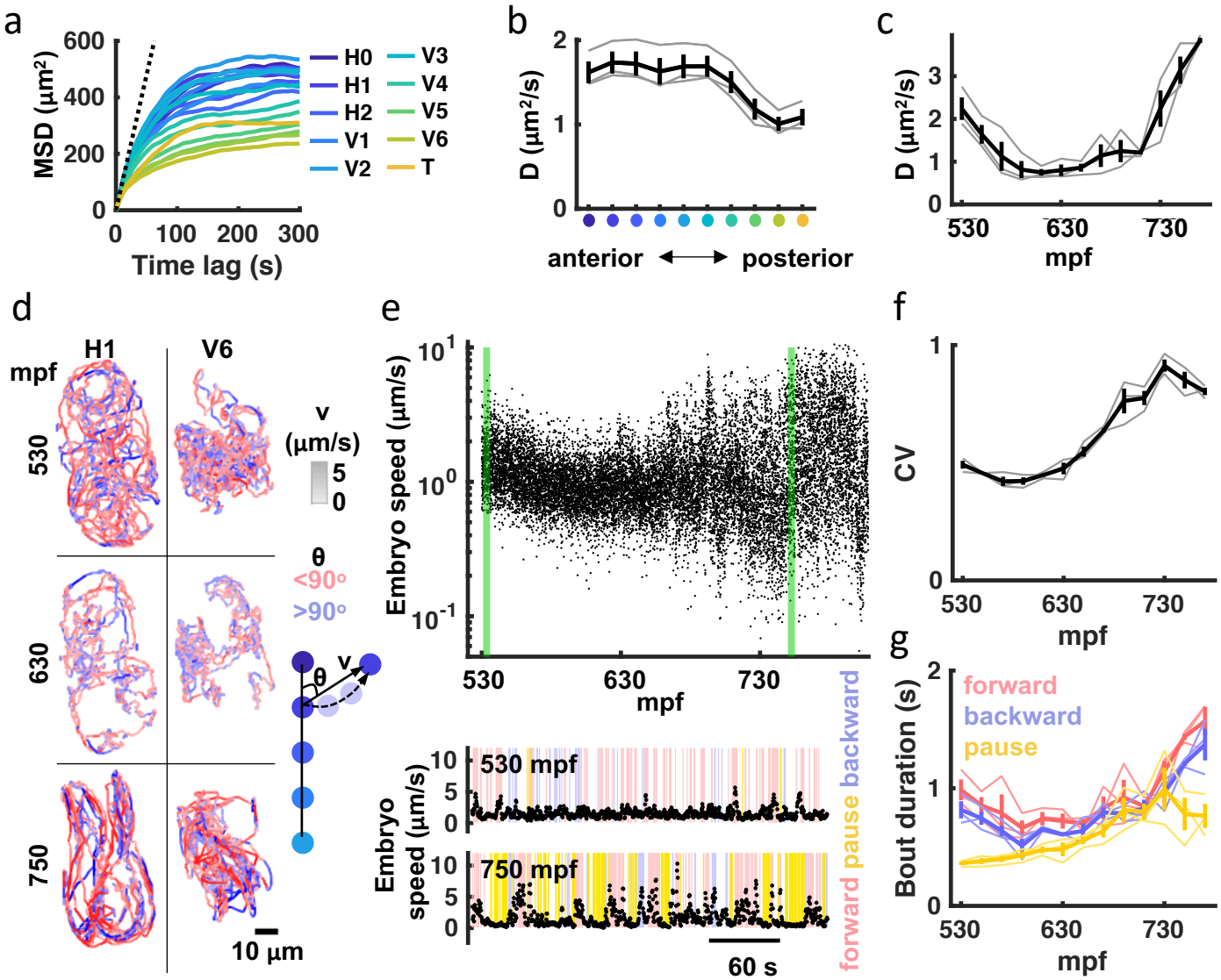
a
MSD (μm²)
600
400
200
0
0
100
200
300
Time lag (s)
H0
H1
H2
V1
V2
V3
V4
V5
V6
T
b
D (μm²/s)
2
1
0
anterior
posterior
c
D (μm²/s)
3
2
1
0
530
630
730
mpf
d
H1
V6
mpf
530
630
750
v
(μm/s)
5
0
θ
<90°
>90°
v
θ
10 μm
e
Embryo speed (μm/s)
10¹
10⁰
10⁻¹
530
630
730
mpf
Embryo speed (μm/s)
530 mpf
750 mpf
10
5
0
60 s
forward
pause
backward
f
CV
1
0
530
630
730
mpf
g
Bout duration (s)
2
1
0
forward
backward
pause
530
630
730
mpf

Fig. 3.

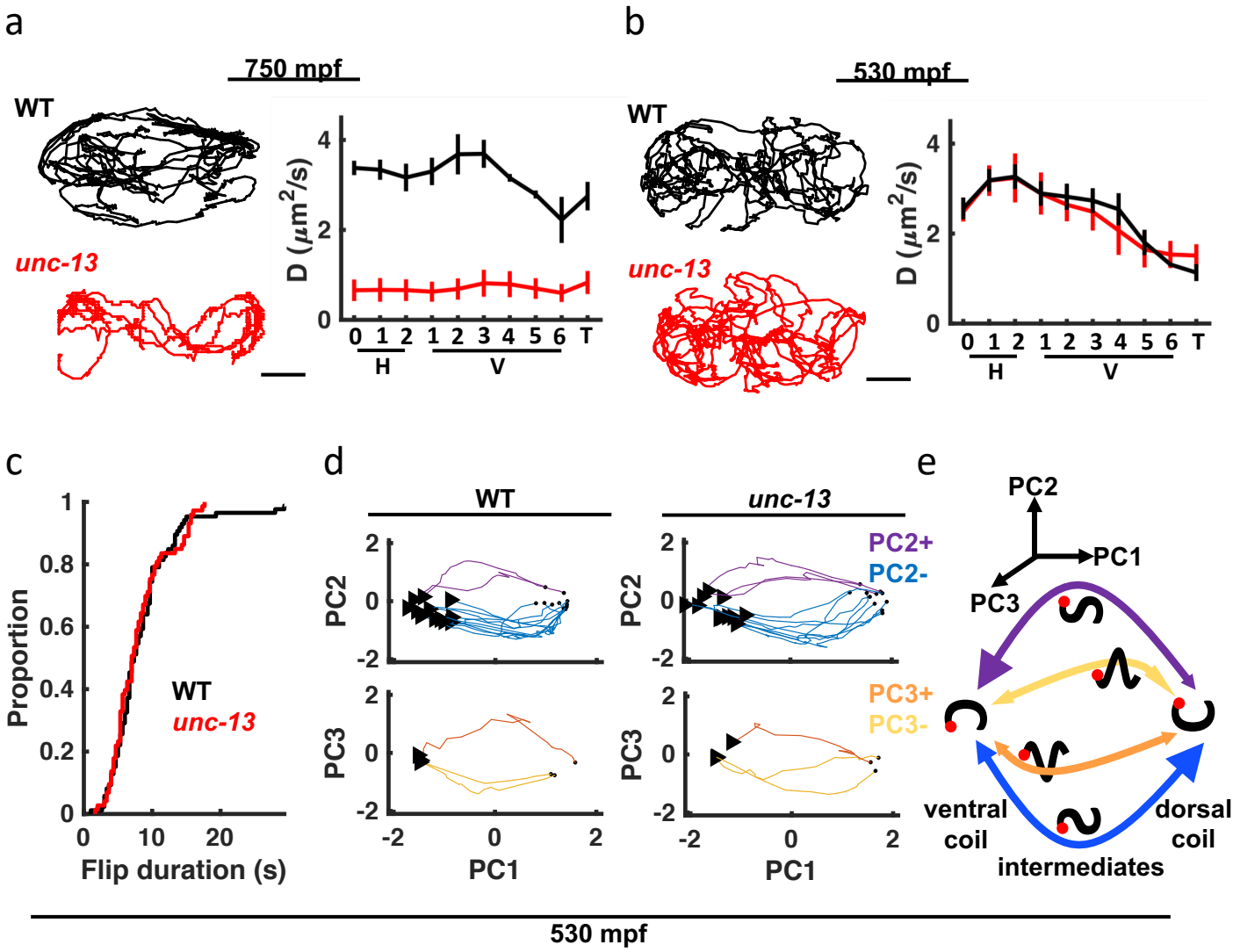
a
750 mpf
WT
unc-13
D (μm²/s)
0 1 2 1 2 3 4 5 6 T
H
V
b
530 mpf
WT
unc-13
D (μm²/s)
0 1 2 1 2 3 4 5 6 T
H
V
c
Proportion
Flip duration (s)
WT
unc-13
d
WT
unc-13
PC2
PC3
PC1
PC2+
PC2-
PC3+
PC3-
e
PC2
PC1
PC3
ventral coil
dorsal coil
intermediates
530 mpf

Fig. 4.

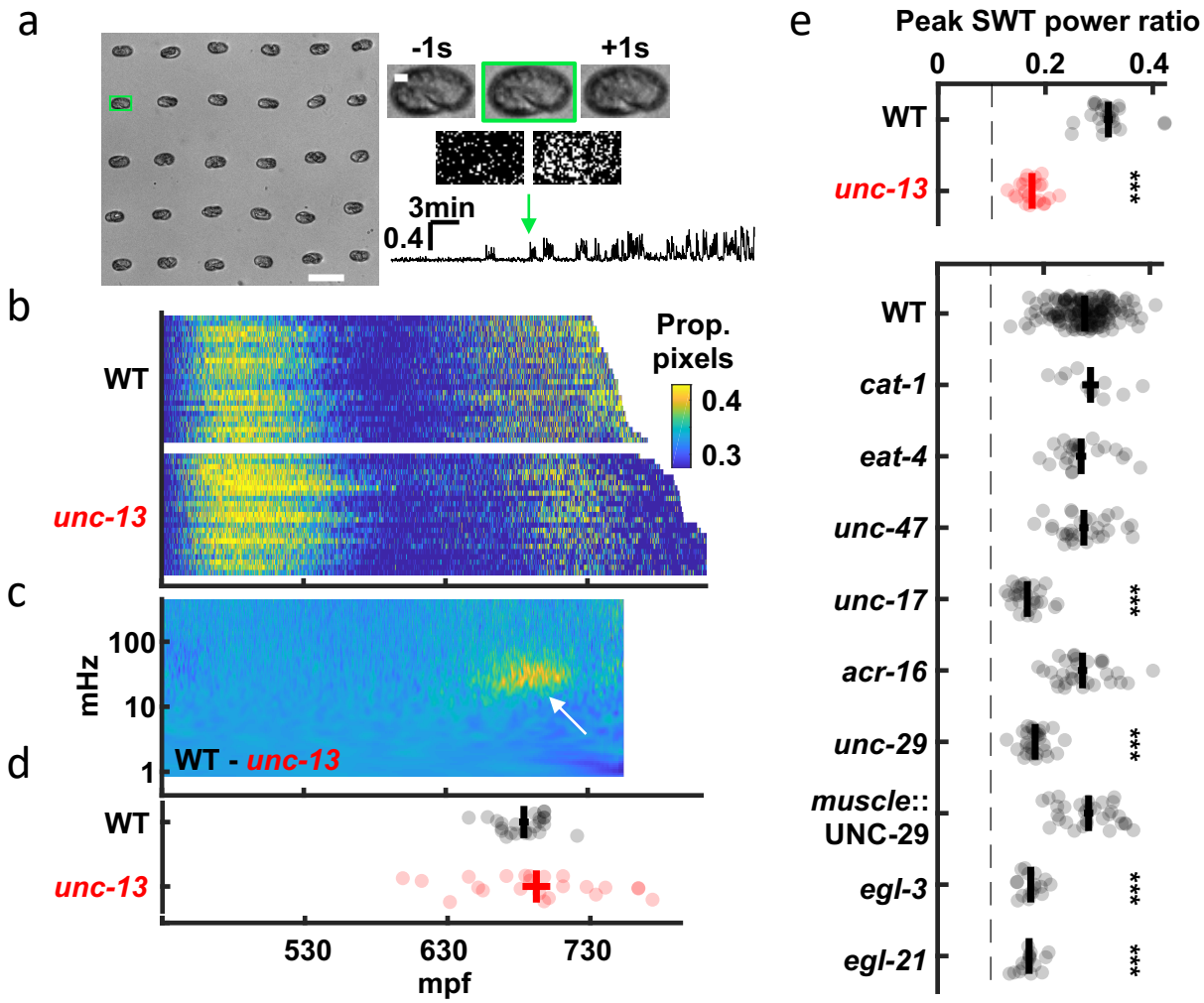
a
-1s
+1s
3min
0.4
b
WT
unc-13
Prop. pixels
0.4
0.3
c
mHz
100
10
1
WT - unc-13
d
WT
unc-13
530
630
730
mpf
e
Peak SWT power ratio
0
0.2
0.4
WT
unc-13
***
WT
cat-1
eat-4
unc-47
unc-17
***
acr-16
unc-29
***
muscle::
UNC-29
egl-3
***
egl-21
***

Fig. 5.

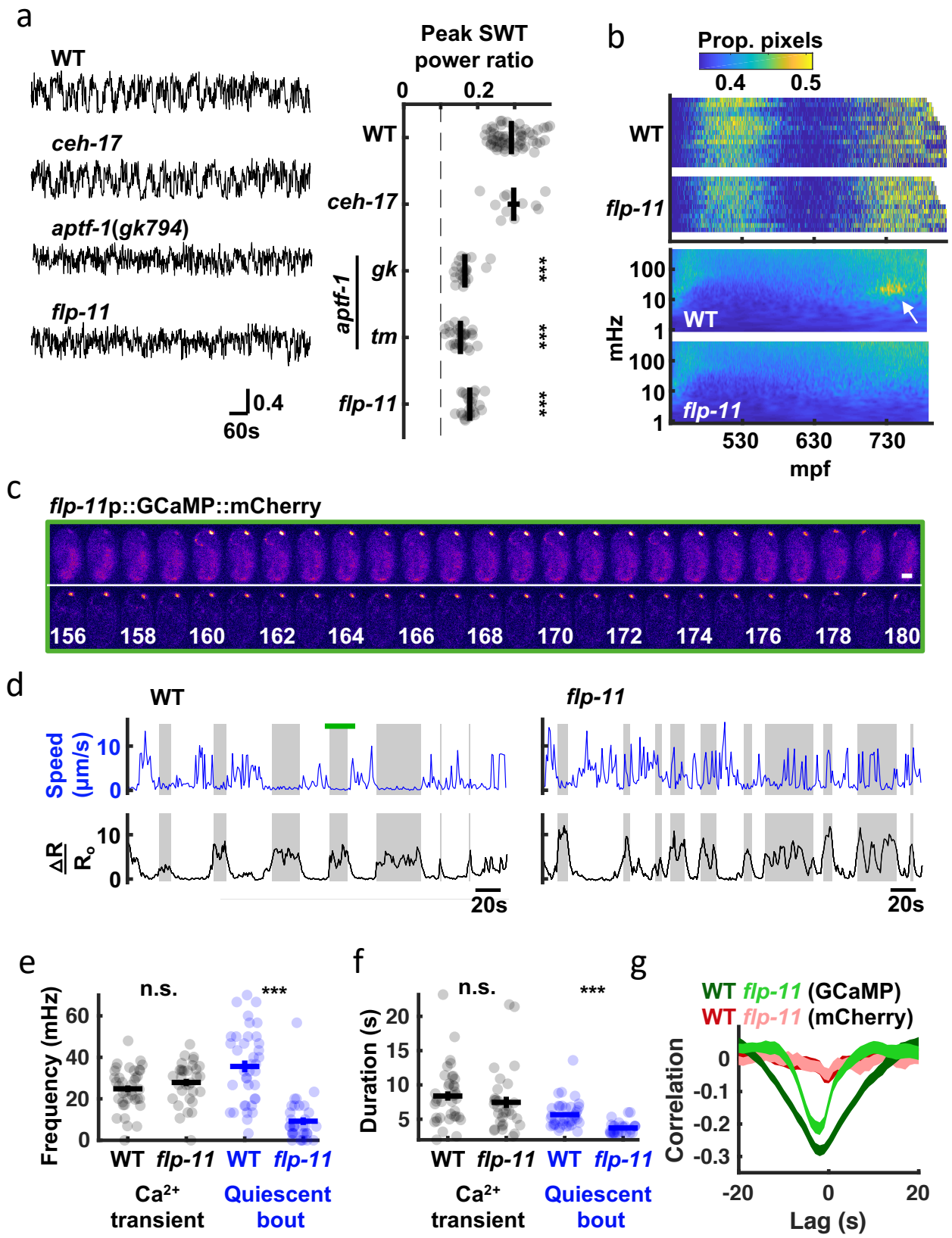
a
WT
ceh-17
aptf-1(gk794)
flp-11
0.4
60s
Peak SWT power ratio
0
0.2
WT
ceh-17
aptf-1
gk
tm
flp-11
***
b
Prop. pixels
0.4
0.5
WT
flp-11
mHz
100
10
1
530
630
730
mpf
c
flp-11p::GCaMP::mCherry
156
158
160
162
164
166
168
170
172
174
176
178
180
d
WT
flp-11
Speed (μm/s)
ΔR/R0
20s
e
Frequency (mHz)
n.s.
***
WT
flp-11
Ca2+ transient
Quiescent bout
f
Duration (s)
g
WT flp-11 (GCaMP)
WT flp-11 (mCherry)
Correlation
Lag (s)

Fig. 6.